

# Mass-Metallicity and Star Formation Rate in Galaxies: a complex relation tuned to stellar age<sup>★</sup>

S. Duarte Puertas<sup>1,2</sup>, J. M. Vilchez<sup>2</sup>, J. Iglesias-Páramo<sup>2</sup>, M. Mollá<sup>3</sup>, E. Pérez-Montero<sup>2</sup>, C. Kehrig<sup>2</sup>, L. S. Pilyugin<sup>4,5</sup>,  
and I. A. Zinchenko<sup>6,4</sup>

<sup>1</sup> Département de Physique, de Génie Physique et d'Optique, Université Laval, and Centre de Recherche en Astrophysique du Québec (CRAQ), Québec, QC, G1V 0A6, Canada

e-mail: salvador-manuel.duarte-puertas.1@ulaval.ca

<sup>2</sup> Instituto de Astrofísica de Andalucía - CSIC, Glorieta de la Astronomía s.n., 18008 Granada, Spain

<sup>3</sup> CIEMAT, Avda. Complutense 40, 28040 Madrid, Spain

<sup>4</sup> Main Astronomical Observatory, National Academy of Sciences of Ukraine, 27 Akademika Zabolotnoho St., 03680, Kyiv, Ukraine

<sup>5</sup> Institute of Theoretical Physics and Astronomy, Vilnius University, Sauletekio av. 3, 10257, Vilnius, Lithuania

<sup>6</sup> Faculty of Physics, Ludwig-Maximilians-Universität, Scheinerstr. 1, 81679 Munich, Germany

Received May 4, 2022; accepted May 4, 2022

## ABSTRACT

**Context.** In this work we study the stellar mass – metallicity relation (MZR) of an extended sample of star-forming galaxies in the local Universe and its possible dependence with the star formation rate (SFR).

**Aims.** A sample of ~195000 Sloan Digital Sky Survey (SDSS) star-forming galaxies has been selected up to  $z=0.22$  with the aim of analysing the behaviour of the relation of MZR with respect to SFR and taking into account the age of their stellar populations.

**Methods.** For this sample we have obtained, for the first time, aperture corrected oxygen and nitrogen-to-oxygen abundances (O/H and N/O, respectively) and SFR using the empirical prescriptions from the Calar Alto Legacy Integral Field Area (CALIFA) survey. To perform this study we make use also of the stellar mass of the galaxies and the parameter  $D_n(4000)$  as a proxy of the age of the stellar population.

**Results.** We derive a robust MZR locus, which is found to be fully consistent with the “anchoring” points of a selected set of well studied nearby galaxies with a direct derivation of the chemical abundance. A complex relation between MZR and SFR across the whole range of galaxy mass and metallicity has been observed, where the slope changes seen in the O/H – SFR plane present a pattern which seems to be tuned to the galaxies’ stellar age, and therefore, stellar age has to be taken into account in the stellar mass – metallicity – SFR relation.

**Conclusions.** In order to provide an answer to the question of whether or not the MZR depends on the SFR it is essential to take into account the age of the stellar populations of galaxies. A strong dependence between the MZR and SFR is observed mainly for star-forming galaxies with strong SFR values and low  $D_n(4000)$ . The youngest galaxies of our SDSS sample show the highest SFR measured for their stellar mass.

**Key words.** galaxies: general – galaxies: star forming – galaxies: formation – galaxies: evolution – galaxies: star formation rate – galaxies: aperture corrections – galaxies: metallicity

## 1. Introduction

Since the pioneering work of Lequeux et al. (1979), a plethora of papers have studied the relation between metallicity and galaxy stellar mass, as well as with other fundamental parameters of galaxies (e.g. Vila-Costas & Edmunds 1992; Garnett 2002; Pilyugin et al. 2004; Tremonti et al. 2004; Lee et al. 2006; Zahid et al. 2014; Sánchez et al. 2017; Maiolino & Mannucci 2019; Sánchez 2020). In all of these works a clear correlation between total stellar mass ( $M_*$ ) and metallicity of galaxies was highlighted. The mass-metallicity relation (MZR) thus remains a key ingredient for our understanding of the formation and evolution of galaxies. Theoretical models predict a tight relation (e.g. Mouhcine et al. 2008; Sakstein et al. 2011; Davé et al. 2011;

Romeo Velonà et al. 2013; Okamoto et al. 2017; De Rossi et al. 2017; Torrey et al. 2018) illustrating how galaxy evolution is driven by galaxy mass, modulated by gas accretion and outflows.

The MZR reaches a maximum near saturation at the high mass end ( $\log(M_*/M_\odot) \geq 10.5$ ), maintaining in a metallicity asymptotically close to the oxygen yield (e.g. Pilyugin et al. 2007). The study of this relation for galaxies of different masses can be used to better ascertain if the MZR could be emerging from a local relationship within galaxies or rather represents a truly global scale relation, e.g. linked to galaxy mass. The overall shape of the MZR is believed to respond mainly to the action of galactic winds and enriched outflows in addition to metal astration driven by star formation and galaxy stellar mass, but other processes related to e.g. galaxy downsizing or massive gas accretion and star formation can be also involved (e.g. Finlator & Davé 2008).

Star formation rate (SFR) was originally introduced as a secondary parameter of the MZR aiming at reducing the observed scatter, and in this way the so-called fundamental mass – metal-

<sup>★</sup> Table 1 with the values of oxygen and nitrogen-to-oxygen abundance ratios for ~195000 SDSS star-forming galaxies and related relevant data is only available in electronic form at the CDS via anonymous ftp to cdsarc.u-strasbg.fr (130.79.128.5) or via <http://cdsweb.u-strasbg.fr/cgi-bin/qcat?J/A+A/>.

licity – SFR relation was defined (MZSFR; e.g. Ellison et al. 2008; Mannucci et al. 2010; Lara-López et al. 2010b). In this fundamental relation, at a fixed galaxy stellar mass, SFR anti-correlates with metallicity, similarly to the predictions of some models about this possible secondary dependence of MZR with SFR (e.g. Dayal et al. 2013). An intense debate (e.g. Sánchez et al. 2013, 2017, 2019; Salim et al. 2014; Barrera-Ballesteros et al. 2017; Cresci et al. 2019) has developed since then about the existence or not of this second dependence on SFR. The observations of a large number of galaxies obtained with integral field spectroscopy (IFS) in CALIFA (Sánchez et al. 2012; García-Benito et al. 2015), and MANGA (Bundy et al. 2015) surveys, or with integrated spectra by Hughes et al. (2013), reach to different conclusions which prevent to understand the exact role played by the SFR, and the possible evolution of MZSFR with redshift.

One of the key differences among the above cited studies, which we face in the present work, is that the integrated galaxies analysis have been usually performed using bright emission lines measured on single aperture spectroscopy of galaxies (e.g. spectra SDSS, VVDS, zCOSMOS, DEIMOS) to derive the oxygen abundance (O/H) of the ionised gas, as a proxy of galaxy metallicity; and the SFR estimates for these galaxies were also derived from the same aperture spectral information, with present-day SFRs often computed from the luminosity of H $\alpha$  emission. The aperture corrections are produced by incomplete or partial coverage of the observed galaxies (e.g. SDSS 3 arcsec fibre spectroscopy), and may produce critical effects, which must be corrected. IFS of a large sample of galaxies of CALIFA has provided the method to correct the emission lines by aperture and spatial sampling effects (Mast et al. 2014; Gomes et al. 2016; Iglesias-Páramo et al. 2016). It has been shown that aperture effects translate in clear flux deficits which, in the case of e.g. SFR, imply corrections of up to  $\sim 0.6$  dex (Iglesias-Páramo et al. 2013; Duarte Puertas et al. 2017); whereas model-based aperture corrections do not solve this problem. In the case of the emission-line fluxes the situation is not trivial, as they, and their corresponding extinction must be aperture corrected before deriving SFR or the different abundance ratios. In particular, differential extinction correction across the disks of galaxies can not be overlooked. In Iglesias-Páramo et al. (2016) empirically CALIFA based aperture corrections are provided for the relevant lines.

The SFR of galaxies can be also derived using multiparametric fitting of their spectral energy distribution, using evolutionary population synthesis models and inverting population synthesis equations (with their own uncertainties). Recent spatially resolved studies using this last technique found a clear correlation between O/H and SFR using the IFS CALIFA and MANGA data (e.g. Cresci et al. 2019). However, according to Sánchez (2020), whether or not a fundamental metallicity relation exists depends on the analysis of the data, i.e., with the same CALIFA data set, Salim et al. (2014) found a dependence between the sSFR and the metallicity not found by Sánchez et al. (2013), who suggested that the MZSFR relation is an artifact of spectroscopy aperture bias. On the other hand, Cresci et al. (2019) concluded that the method used to calculate the stellar mass of galaxies, the other key ingredient in the MZR, also affects the obtained results. To these considerations we need to add that other research using IFS studied the relationship between O/H and other parameters (e.g. Barrera-Ballesteros et al. 2018, 2020; Sánchez-Menguiano et al. 2020) propose that there might be some dependence, even indirectly, between gas-phase metallicity and stellar age at local and global scales. Both questions are actually related, thus the

study of a possible evolution of the zero point and slope of the MZR with cosmic time and its dependence on SFR, can shed light on how galaxies formed, were assembled and evolve, an also on the infall and galactic wind phases of their chemical evolution. The MZR has been extensively studied as a general scaling relation of star-forming galaxies in the local Universe (e.g. Mannucci et al. 2010; Lara-López et al. 2010b; Kashino et al. 2016; Curti et al. 2020), as a function of galaxy environment (e.g. Ellison et al. 2009; Petropoulou et al. 2011, 2012; Peng & Maiolino 2014; Pilyugin et al. 2017), and in medium and high redshift surveys (e.g. Brown et al. 2016; Hunt et al. 2016; Kojima et al. 2017). Some evolution is expected for the shape or for the zero point of the MZR (e.g. Lara-López et al. 2010a; Møller et al. 2013; Pilyugin et al. 2013); though, other works find no significant evolution for the MZSFR (e.g. Mannucci et al. 2010; Cresci et al. 2012).

Besides the above uncertainties, we have the well known issue of metallicity derivation from spectroscopy in large samples, which has been discussed elsewhere (e.g. Curti et al. 2017, and references therein). Since temperature sensitive lines fluxes are not available for the huge majority of these objects (e.g. in SDSS), abundance calibrations are applied to derive their metallicity. Not all abundance calibrations appear equally reliable when they are compared with oxygen abundances derived from the direct method. In fact, recent abundance calibrations empirically calibrated provide an abundance which, statistically, is typically within 0.2 dex uncertainty of the direct value. In this respect, some support can be gained using complementary versions of the MZR relation, e.g. using stellar metallicity derived either from integrated young stellar populations (e.g. Gallazzi et al. 2005) or for individual massive stars (e.g. Bresolin et al. 2016); or deriving O/H directly from stacked spectra of mass-grouped star-forming galaxies (e.g. Andrews & Martini 2013); also, replacing O/H by nitrogen-to-oxygen abundance (N/O), an abundance ratio less dependent on electron temperature and a well known “chemical clock” (e.g. Edmunds & Pagel 1978; Pilyugin et al. 2003; Mollá et al. 2006) adding useful chemical evolution information. N/O also presents a well-known relation with stellar mass (Pérez-Montero & Contini 2009), as for high metallicity nitrogen has mainly a secondary origin, and as its derivation does not depend on the excitation of the gas, the study of the mass vs N/O relation (MNOR) can thus be very useful to better understand the zero-point and the slope of the MZR. In addition the combined study of mass, SFR, and N/O can also be used to better discriminate the dependence of metallicity with SFR. In this work, the caveats mentioned above have been taken into account for the metallicity derivation and analysis, and the corresponding sanity checks have been performed when appropriate.

In summary, in order to carry out an in depth study of the relation between MZR and SFR, we must address the systematic effects involved, as discussed in Telford et al. (2016) and Cresci et al. (2019), as those associated to e.g. signal-to-noise ratio (S/N), aperture effects, or the metallicity indicators used, among others, which can affect the derivation of the MZR and any possible dependence of MZR with SFR. This is the main objective of this work. To do it, we benefit from the methodology and knowledge gained with the CALIFA survey and apply it here to minimise systematic effects. Hence we examine in detail the behaviour of the relation between MZR and SFR for a large and complete sample of SDSS star-forming galaxies (see Duarte Puertas et al. 2017, for details) using the total fluxes of their emission lines empirically corrected by extinction and aperture effects in a consistent manner. We will analyse the MZR and

SFR relationships, studying in particular the role of the age, using the parameter  $D_n(4000)$  as a proxy, of the stellar populations of galaxies.

The structure of this paper is organised as follows: in Sect. 2 we describe the data providing a description of the methodology used to select the sample (Sect. 2.1). The methodology followed to derive all the parameters used in this work is presented in Sect. 2.2. Main results and discussion are given in Sect. 3. Conclusions are given in Sect. 4. Finally, supplementary material has been added in Appendix A. Throughout the paper, we assume a Friedman-Robertson-Walker cosmology with  $\Omega_{\Lambda 0} = 0.7$ ,  $\Omega_{m0} = 0.3$ , and  $H_0 = 70 \text{ km s}^{-1} \text{ Mpc}^{-1}$ . We use the Kroupa (2001) universal initial mass function (IMF).

## 2. Data and sample

### 2.1. The sample of galaxies

Our study is based on the catalogue of 209276 star-forming galaxies extracted from SDSS-DR12 (Alam et al. 2015) and presented in Duarte Puertas et al. (2017). The galaxies span a redshift ( $z$ ) and stellar mass ranges of  $0.005 \leq z \leq 0.22$  and  $8.5 \leq \log(M_*/M_\odot) \leq 11.5$ , respectively. All the emission line fluxes (i.e. [OII] $\lambda\lambda$  3727, 3729, [OIII] $\lambda$  5007, H $\beta$ , [NII] $\lambda$  6584, and H $\alpha$ ),  $\log(M_*/M_\odot)$ ,  $z$ , and  $D_n(4000)$ <sup>1</sup> used in this work have been taken from Max-Planck-Institut für Astrophysik and Johns Hopkins University (MPA-JHU) public catalogue<sup>2</sup> (Kauffmann et al. 2003; Brinchmann et al. 2004; Tremonti et al. 2004; Salim et al. 2007). From this catalogue we have selected a subset of 194353 SDSS star-forming galaxies according to the following criteria:

- i)  $z \geq 0.02$ . Due to the SDSS spectral range (3800-9200 Å), this is the minimum redshift required to include and measure [OII] $\lambda\lambda$  3727, 3729; this emission lines are necessary to derive the metallicity (see Sect. 2.2) from our spectra (Pilyugin et al. 2012; Pérez-Montero et al. 2013).
- ii) A S/N  $\geq 3$  is imposed for all the line fluxes used to derive O/H and N/O.

For these objects, we will determine the oxygen and nitrogen-to-oxygen abundances, following the prescriptions explained in Sect. 2.2. For the SFR, we use aperture corrected measurements from the database of Duarte Puertas et al. (2017).

### 2.2. Empirical aperture correction and chemical abundances

It is well known that the 3 arcsec diameter fibres in SDSS only cover a limited region of galaxies in the low- $z$  Universe ( $z < 0.22$ ). In order to obtain the total SFR for all the galaxies in our sample we have used the aperture corrected SFR values from Duarte Puertas et al. (2017), where a detailed description of the aperture correction for the H $\alpha$  flux measurements in SDSS is presented.

The aperture corrections for the H $\alpha$  flux and  $\log([OIII]\lambda 5007/H\beta)$ ,  $\log([NII]\lambda 6584/H\alpha)$ , and H $\alpha/H\beta$  flux ratios in our sample were performed using the prescriptions by Iglesias-Páramo et al. (2016). These corrections were derived for a sample of disk galaxies in the CALIFA survey, representative of different types and masses (Iglesias-Páramo et al. 2016).

The aperture correction recipe for [OII] $\lambda\lambda$  3727, 3729 has been also provided to us (by Iglesias-Páramo et al., private communication). Conversely, as shown in Belfiore et al. (2016), the  $D_n(4000)$  break strength index remains substantially constant across star-forming galaxies, given that their young stellar component appears well distributed through out all the galactic disk; hence no aperture correction was applied for it. In summary, for each galaxy in our sample, the line fluxes measured in the SDSS fibres (i.e. [OII] $\lambda\lambda$  3727, 3729, [OIII] $\lambda$  5007, H $\beta$ , [NII] $\lambda$  6584, and H $\alpha$ ) were corrected for extinction following Duarte Puertas et al. (2017), and then they were aperture-corrected applying the equations in Table 20 of Iglesias-Páramo et al. (2016). These emission line fluxes are necessary for the derivation of oxygen and nitrogen abundances, as explained.

In order to derive the metallicity of our sample galaxies, given that the faint temperature sensitive lines are not available, we must rely on bright lines abundance calibrations (including from [OII], [OIII] to [NII]). It is well known that some calibrations produce different absolute values of O/H; especial care has been exercised in this work in the selection of the abundance calibrations applied. We have used three different methods:

1. We first follow the study updated by Curti et al. (2017) for O/H derivation and have selected their calibration of O3N2 which presents the wider O/H prediction range with the smallest dispersion.
2. In addition, we have also adopted the empirical calibrations by Pilyugin & Grebel (2016) for nitrogen (their eq. 13) and oxygen (their eqs. 4, 5) abundances.

All these calibrations are empirical, i.e. they are calibrated against direct abundances calculated with electron temperature measurements. Finally, we have used the ones given by the code HII-CHI-MISTRY (Pérez-Montero 2014), based on photoionization models, and which reproduce chemical abundances consistent with their corresponding direct derivations<sup>3</sup>. For the sake of consistency to compare with previous and other works performed including spectroscopy of distant galaxies, oxygen and nitrogen-to-oxygen abundances for our sample galaxies have been derived with the three methods mentioned above once they are free from aperture effects (given that the emission line fluxes used were all aperture corrected), corresponding to the entire galaxy. We have also derived the value of oxygen and nitrogen-to-oxygen abundances in fibre and we have obtained that the values derived in the fibre, for O/H and N/O, are systematically higher than those aperture corrected. The mean oxygen abundance difference between the fibre and the value corrected for aperture,  $\Delta(12+\log(O/H))$ , is 0.04 dex (the standard deviation is 0.01 dex) for our sample of star-forming galaxies. In the case of the mean nitrogen-to-oxygen abundance difference,  $\Delta(\log(N/O))$ , we have found a value of 0.06 dex (the standard deviation is 0.01 dex). All the abundances obtained for each object resulted consistent within the errors, and overall, the three abundance outputs from the calibrations selected (and values in the fibre) are statistically consistent to within  $\sim 0.15$  dex; with the higher consistency and lowest errors being achieved especially for the nitrogen to oxygen abundance ratio. Taking this fact into account, in this work we adopt for each galaxy as representative the O/H and N/O abundances obtained applying Pilyugin & Grebel (2016). As a result, we have compiled Table 1 where we show a sample of the online table of 194353 star-forming galaxies, where their fluxes have been aperture-corrected, for which

<sup>1</sup>  $D_n(4000)$  corresponds to the narrow definition of the 4000 Å break strength from Balogh et al. 1999 that can be considered a proxy of stellar population age.

<sup>2</sup> Available at <http://www.mpa-garching.mpg.de/SDSS/>.

<sup>3</sup> A known feature is that most photoionisation model abundances are typically overestimated; while HII-CHI-MISTRY abundances appear consistent with direct derivations



**Table 1.** Compiled data for our sample of star-forming galaxies. The whole table is available in electronic format.

(1) specObjID	(2) $12+\log(\text{O}/\text{H})$	(3) $\log(\text{N}/\text{O})$	(4) $\log(\text{M}_\star)$ [ $\text{M}_\odot$ ]	(5) $\log(\text{SFR})$ [ $\text{M}_\odot \text{ yr}^{-1}$ ]	(6) $\text{D}_n(4000)$
1399656635961468928	$8.44 \pm 0.07$	$-1.23 \pm 0.11$	$9.98^{+0.15}_{-0.12}$	$0.86 \pm 0.02$	$1.45 \pm 0.17$
1302792405518411776	$8.16 \pm 0.07$	$-1.38 \pm 0.06$	$9.95^{+0.32}_{-0.47}$	$-0.28 \pm 0.01$	$1.21 \pm 0.03$
1302813296239339520	$8.38 \pm 0.02$	$-1.17 \pm 0.02$	$10.23^{+0.33}_{-0.48}$	$0.32 \pm 0.01$	$1.19 \pm 0.03$
1398489229004138496	$8.53 \pm 0.02$	$-0.79 \pm 0.05$	$10.64^{+0.11}_{-0.08}$	$1.45 \pm 0.01$	$1.20 \pm 0.03$
1399648389624260608	$8.40 \pm 0.01$	$-1.10 \pm 0.02$	$9.51^{+0.13}_{-0.08}$	$0.34 \pm 0.01$	$1.12 \pm 0.05$
...	...	...	...	...	...

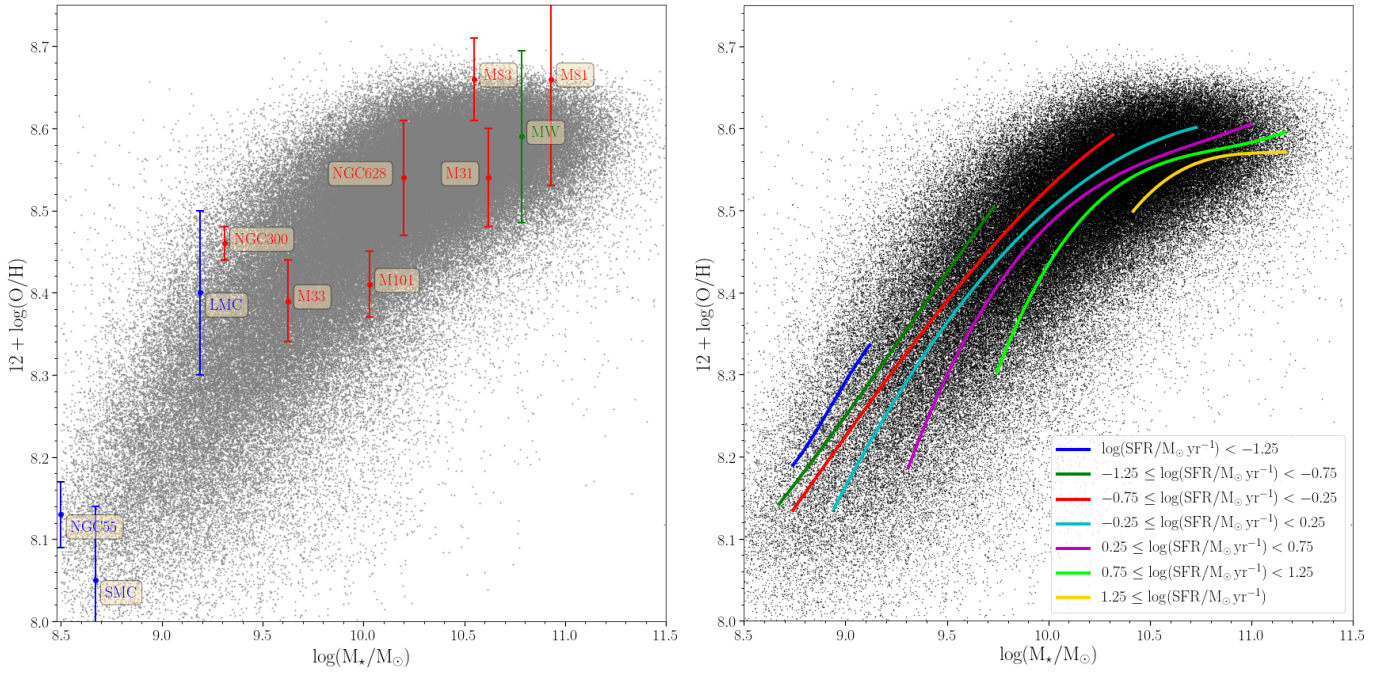


**Fig. 1.** a) Aperture corrected MZR. Star-forming galaxies of our sample (grey dots), as well as the Milky Way (green mark) and other nearby galaxies (labelled; coloured points) with direct (from electron temperature) oxygen abundances are shown. Blue or red colour indicate galaxies with a flat or non-zero radial oxygen gradient, respectively. *References as follows: galaxy name, O/H reference, stellar mass reference; SMC, LMC, and M81, Bresolin et al. (2016), Kudritzki et al. (2012); NGC 55, Magrini et al. (2017), Lee et al. (2006); MW, Fernández-Martín et al. (2017); Arellano-Córdova et al. (2021), Licquia & Newman (2015); M83, Bresolin et al. (2016); Hernandez et al. (2019), Kang et al. (2016); M33 and NGC 300, Bresolin et al. (2016); Kang et al. (2016); M 31, Zurita & Bresolin (2012), Fisher & Drory (2011); M 101, Croxall et al. (2016), Skibba et al. (2011); NGC 628, Berg et al. (2015), Cook et al. (2014) (see also Vilchez et al. 2019).* b) Relation between  $12+\log(\text{O}/\text{H})$  and  $\text{M}_\star$  for SDSS star-forming galaxies, grey points. Overplotted blue, green, red, cyan, magenta, lime, and yellow solid lines represent the fits to the running median of the SFR of the galaxies, calculated in bins of 1000 galaxy points, corresponding to seven SFR intervals as indicated.

we have the spectroscopic identifier from SDSS (specObjID), oxygen, as  $12+\log(\text{O}/\text{H})$ , and nitrogen-to-oxygen abundance ratio, as  $\log(\text{N}/\text{O})$ , abundances, stellar mass, as  $\log(\text{M}_\star/\text{M}_\odot)$ , the SFR (in  $\text{M}_\odot \text{ yr}^{-1}$  units), and the parameter  $\text{D}_n(4000)$  that we use as the stellar population age indicator. Table 1 also shows the uncertainties for each property considered.<sup>4</sup>

### 3. Discussion

In Fig. 1, panel a, we show the oxygen abundance,  $12+\log(\text{O}/\text{H})$ , versus total stellar mass for the 194353 galaxies in our sample, which clearly reproduce the MZR relation. A further quality

check of our MZR derivation can be done comparing it with the oxygen abundance and total stellar mass<sup>5</sup> for the Milky Way<sup>6</sup> and ten well known nearby galaxies for which precise abundance values of their HII regions have been derived using the direct method from available electron temperature measurements. These nearby galaxies show well defined spatially resolved radial abundance gradients, thus their representative abundance, corresponding to the integrated galaxy flux can be easily derived using the IFS measurements in the CALIFA survey. To

<sup>4</sup> The uncertainties of  $\log(\text{M}_\star/\text{M}_\odot)$  and  $\text{D}_n(4000)$  have been taken from MPA-JHU.

<sup>5</sup> NGC 55, NGC 300, and M 33 stellar masses transformed from Chabrier (2003) to Kroupa (2001) IMF dividing by 0.943 (Mannucci et al. 2010).

<sup>6</sup> An effective radius face value of 5.9 kpc was assumed for the Milky Way (Sackett 1997; Yin et al. 2009).



do so we use the O/H measured in the characteristic radius ( $0.4 \times R_{25}$ , basically similar to the effective radius of the galaxy, e.g. [Sánchez et al. 2013](#)), the most suitable representative value of the whole galaxy abundance. According to [Sánchez et al. \(2013\)](#), for galaxies presenting  $12 + \log(\text{O}/\text{H})$  abundance at the effective radius,  $12 + \log(\text{O}/\text{H})_{\text{Reff}} \leq 8.6$  dex, the mean difference between  $12 + \log(\text{O}/\text{H})$  of the integrated galaxy flux and  $12 + \log(\text{O}/\text{H})_{\text{Reff}}$  is  $\sim -0.03$  dex; whereas for galaxies with  $12 + \log(\text{O}/\text{H})_{\text{Reff}}$  above 8.6 dex, this difference amounts to  $\sim 0.06$  dex. We have applied this conversion to calculate the representative  $12 + \log(\text{O}/\text{H})$  abundances of our selected nearby galaxies; these objects are also shown in Fig. 1 panel a. It can be seen that the selected sample of nearby galaxies and our sample of SDSS star-forming galaxies show an excellent agreement delineating the local universe MZR, free from aperture effects, derived in this work. As mentioned in Section 2.2, we have derived (and compared) the O/H values using the empirical calibrations from [Pilyugin & Grebel \(2016\)](#); [Pérez-Montero & Contini \(2009\)](#), the direct method by using the electron temperature for objects with auroral line measurements, and the theoretical photoionisation models (HII-CHI-mistry) from [Pérez-Montero \(2014\)](#). All these methods lead to overall consistent abundances -within the errors- and the differences between them have already been discussed. In Fig. A.1 it can be seen that all galaxies where the electron temperature has been calculated show a high consistency between the O/H from the direct method and the corresponding values obtained in this work using empirical calibrators. Therefore we consider that the oxygen abundances used are precisely estimated and better than others in the literature.

As we also want to see the role of the SFR in the MZR relation, we show in panel b) of Fig. 1 the diagram for the same MZR as in panel a), but overplotting the lines representing the fits to the running medians of seven different SFR intervals. The strong correlation between oxygen abundance and galaxy stellar mass, shown in the MZR plot, is also evident in all the shown SFR lines separately. We can see also how these iso-SFR loci tend to saturate at higher abundances and level off near solar metallicity<sup>7</sup>. We may also see that for a fixed  $\log(M_*/M_\odot)$ , galaxies with a higher metallicity present lower SFR than lower metallicity galaxies, in line with previous findings (e.g. [Mannucci et al. 2010](#)).

We now analyse the relationship between the abundances and the SFR. In panel a) of Fig. 2, we show our aperture corrected oxygen abundances, as  $12 + \log(\text{O}/\text{H})$ , versus the SFR for the galaxy sample (grey points) following the same statistical procedure as in the previous figure. We computed the running medians for six intervals of  $\log(M_*/M_\odot)$  with  $\Delta \log(M_*/M_\odot) = 0.5$  dex each (see also Figure A.2). Their corresponding fits are plotted by black-dotted lines. The total covered range in galaxy stellar mass is  $8.5 \leq \log(M_*/M_\odot) \leq 11.5$  in both panels. The overlaid colour dashed lines show the fits to the running median of the  $D_n(4000)$  index of the sample galaxies, calculated for six intervals from  $D_n(4000) < 1.1$  to  $D_n(4000) \sim 1.5$ , with  $\Delta D_n(4000) = 0.1$  dex each, as indicated in the plot; in parenthesis the total number of points per interval is quoted. We can see a clear overall trend between  $12 + \log(\text{O}/\text{H})$  against SFR in our sample (grey points). In panel b) of the same Fig. 2 we similarly show the aperture corrected  $\log(\text{N}/\text{O})$  versus SFR. There, we have again the  $\log(\text{N}/\text{O})$  versus SFR considering the same galaxy mass and  $D_n(4000)$  bins, and fits to the running median. A similar strong correlation is also present between these two properties. A wide range in  $\log(\text{N}/\text{O})$  is covered by our SDSS

galaxy sample, going from over-solar<sup>8</sup> values to the level typical of low metallicity dwarf galaxies ( $\log(\text{N}/\text{O}) \sim -1.5$ ). All the lines shown in Fig. 2 (i.e. black for stellar mass and coloured for  $D_n(4000)$ ) are representing the real statistical (median) loci of the galaxy points and they are the result of the fit to the statistical distribution of the properties considered (i.e.  $D_n(4000)$ , stellar mass, and O/H) for the SDSS star-forming galaxies sample used in this work.

It is important to bear in mind that  $D_n(4000)$  depends on stellar population age, presenting lowest values for the youngest stellar populations, while the older ones show higher values ([Balogh et al. 1999](#)). In panels a) and b) of Fig. 2 we can see how for a fixed  $\log(M_*/M_\odot)$ , galaxies with lower SFR present systematically higher values of  $D_n(4000)$ , suggesting that they host older stellar populations. For  $D_n(4000) > 1.2$ , we can see that the lines corresponding to the most massive galaxies ( $\log(M_*/M_\odot) > 10.5$ ) tend to saturate, and seem to flatten above  $12 + \log(\text{O}/\text{H}) \geq 8.55$  and  $\log(\text{N}/\text{O}) \geq -0.9$ , irrespective of their SFR. For nearly the entire mass range of the sample ( $\log(M_*/M_\odot) \leq 11$ ), oxygen abundance,  $12 + \log(\text{O}/\text{H})$ , shows a nearly flat or very mild decrease with respect to SFR along the black-dotted lines. Although the usual assumption is that SFR depends on age, showing an anticorrelation between stellar age and SFR when the stellar mass is taken into account, actually we show in this plot that both effects are disentangled. In Fig. 3 we have plotted the SFR as a function of  $D_n(4000)$  to see more clearly this SFR-age effect. In this figure, we see that at face value there is a correlation between high SFR and high  $D_n(4000)$  values. Then, we overplotted the mass isolines and O/H isolines for six stellar mass bins and six O/H ranges, respectively, for our sample of SDSS star-forming galaxies. We can see how: i) at a fixed SFR the corresponding entire range of  $D_n(4000)$  is covered; ii) at fixed stellar mass, the lower the SFR, the higher the  $D_n(4000)$ ; and iii) at fixed O/H we see that the relationship is more complex: from  $D_n(4000) \sim 1.2$  towards the right, for  $\text{O}/\text{H} < 8.5$  the SFR stops decreasing with  $D_n(4000)$ . For the left region, however, the anticorrelation between SFR and  $D_n(4000)$  is very strong. We consider this relationship to be relevant and deserving of further exploration with our sample of star-forming galaxies.

Depending on the stellar mass range, there is a value of SFR for which a change in O/H is observed. This SFR value varies depending on the stellar mass range considered. The iso- $D_n(4000)$  line between [1.1-1.2] accompanies the change in the O/H – SFR relation depending on the stellar mass, which suggests that this line determines a statistical value for stellar mass, SFR, and age.<sup>9</sup> The data do not allow us to say the exactly age where the slope of these iso-mass lines change in the O/H-SFR diagram, but our results allow us to say that it must occur around that  $D_n(4000)$  value (i.e. in the green line). Therefore, in order to address this point, we have proceeded as follows:

- We derived  $\left. \frac{d\text{O}/\text{H}}{d\text{SFR}} \right|_{M_*}$ , i.e. the derivative of O/H versus SFR at constant stellar mass, along all iso-mass lines below the range  $10 \leq \log(M_*/M_\odot) < 10.5$ ; (that means for four iso-mass lines).
- We obtain the value of  $\log(\text{SFR})$  for which the derivative presents the net measurable change,  $\log(\text{SFR}_{\text{deri}})$ , with a minimum value of  $-0.002$ , the half of the value obtained for the

<sup>8</sup> Solar  $\log(\text{N}/\text{O})_\odot = -0.86$  ([Asplund et al. 2009](#); [Tsamis et al. 2011](#)).

<sup>9</sup> This iso- $D_n(4000)$  line around 1.1-1.2, as the others, is derived as the statistical median of galaxies with  $D_n(4000)$  values between 1.1 and 1.2. It is therefore the geometric locus of SDSS star-forming galaxies within these  $D_n(4000)$  values.

<sup>7</sup> Solar metallicity:  $12 + \log(\text{O}/\text{H})_\odot = 8.69$  ([Asplund et al. 2009](#)).

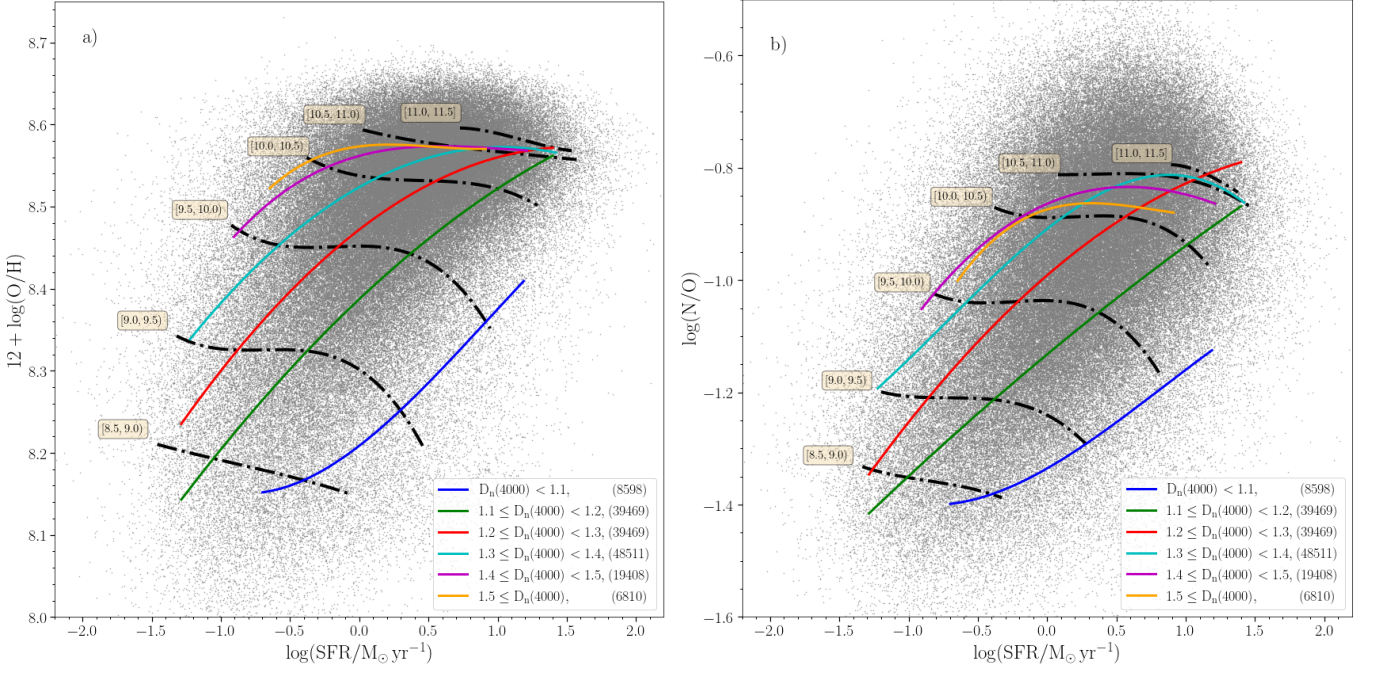


**Fig. 2.** a) Relation between the  $12 + \log(\text{O}/\text{H})$  and SFR corrected for aperture for star-forming galaxies. Blue, green, red, cyan, magenta, and yellow solid lines represent the fits to the running median for bins of 1000 objects in six  $D_n(4000)$  bins. The number of star-forming galaxies in each  $D_n(4000)$  bin appear on the legend. Black dash dotted lines show the  $12 + \log(\text{O}/\text{H})$  vs. SFR values of the running median fits for bins of 1000 objects in six  $\log(M_{\star}/M_{\odot})$  bins (each box shows the considered  $\log(M_{\star}/M_{\odot})$  range). b) Relation between the  $\log(\text{N}/\text{O})$  and SFR for star-forming galaxies (colours and numbers of star-forming galaxies in each  $D_n(4000)$  bins as in a).

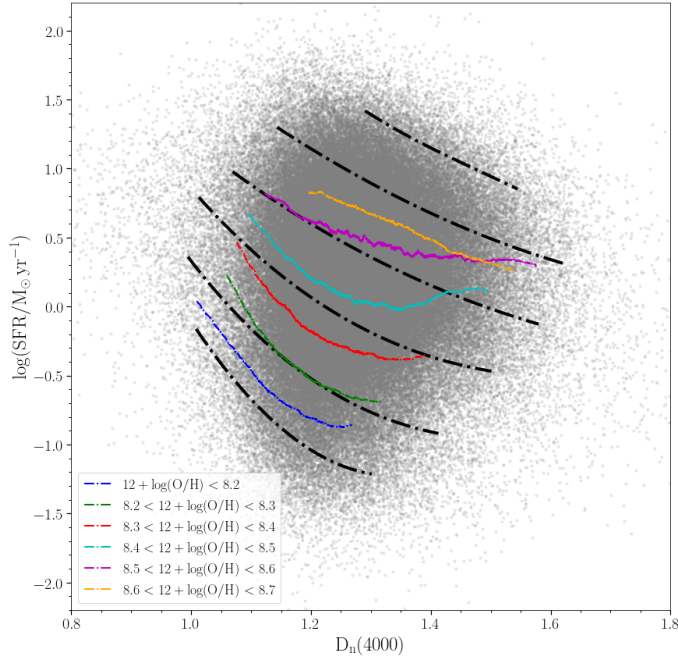


**Fig. 3.** Relation between the SFR and  $D_n(4000)$  for our sample of star-forming galaxies. Blue, green, red, cyan, magenta, and yellow solid lines represent the running median for bins of 2000 objects in six O/H bins. Black dash dotted lines show the fit to the running median for bins of 1000 objects in six  $\log(M_{\star}/M_{\odot})$  bins, from low stellar mass (8.5, lower part of the figure) to high stellar mass (11.5, higher part of the figure).

iso-mass line of the range  $8.5 \leq \log(M_{\star}/M_{\odot}) < 9.0$ ; That is

the point where the slope starts to be steeper (and negative) than this value.

- The iso-mass line corresponding to this lowest mass range plotted shows a nearly constant derivative, approximately a straight line in the plot without any apparent change in its slope; therefore, any change in the derivative of this iso-mass line should have occurred for  $\log(\text{SFR}) < -1.5$  (alternatively, there exists no such change in the derivative of the sub-sample of SDSS galaxies in these stellar mass and SFR range or it is small and we cannot statistically “see” it)
- We determine  $\log(\text{SFR}_{\text{cut}})$  as the SFR value at which each iso- $D_n(4000)$  line cut each iso-mass line in the O/H vs. SFR diagram in Fig. 2.
- Then we compute the difference between  $\log(\text{SFR}_{\text{cut}})$  and  $\log(\text{SFR}_{\text{deri}})$ , as  $\Delta \log(\text{SFR}) = \log(\text{SFR}_{\text{cut}}) - \log(\text{SFR}_{\text{deri}})$ , for each iso-mass line. Since the iso- $D_n(4000)$  line between 1.2 and 1.3 does not intersect the  $8.5 \leq \log(M_{\star}/M_{\odot}) < 9.0$  iso-mass line in the O/H vs SFR diagram, we assume the position in this diagram at which it would intersect by extrapolating slightly the iso- $D_n(4000)$  line for the sake of this test.

We show in Fig. 4 the resulting  $\Delta \log(\text{SFR})$  for the different stellar mass ranges we have considered, as a function of the iso- $D_n(4000)$  ages. The symbols are coloured-coded according to the colour of the iso- $D_n(4000)$  lines of Fig. 2. We see as the green points show the closest values to  $\Delta \log(\text{SFR}) = 0$ . The mean value of  $\Delta \log(\text{SFR}) = 0.72, 0.14, -0.35, -0.75$ , and  $-1.02$  for galaxies in the  $D_n(4000)$  ranges  $< 1.1$ ,  $[1.1-1.2]$ ,  $[1.2-1.3]$ ,  $[1.3-1.4]$  and  $[1.4-1.5]$ , respectively. The difference is proportionally larger as we move away from the iso- $D_n(4000)$  with values between 1.1 and 1.2 (green line), i.e., this iso- $D_n(4000)$  line is the one with values of  $\Delta \log(\text{SFR})$  closest to zero in all iso-masses considered in this figure. From this, we may consider



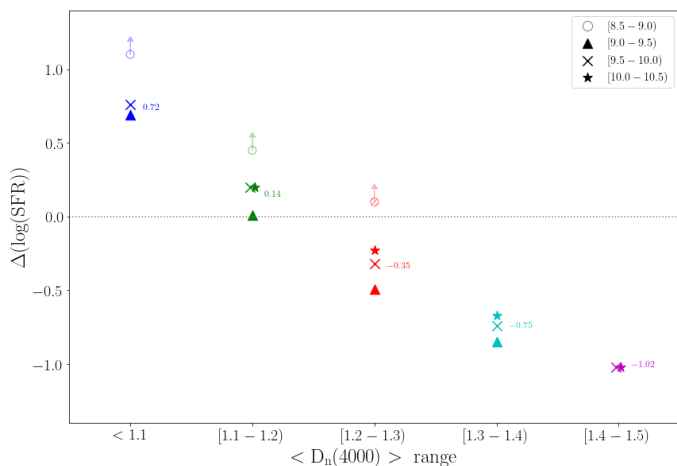


**Fig. 4.** Relation between  $\Delta \log(\text{SFR})$  and the iso- $D_n(4000)$  ranges. The symbols are colour-coded depending on the  $D_n(4000)$  range and according to Fig. 2, being  $D_n(4000) < 1.1$  (blue),  $1.1 \leq D_n(4000) < 1.2$  (green),  $1.2 \leq D_n(4000) < 1.3$  (red),  $1.3 \leq D_n(4000) < 1.4$  (cyan), and  $1.4 \leq D_n(4000) < 1.5$  (magenta). The symbol type is related to  $\log(M_*/M_\odot)$  range considered, as labelled. For the stellar mass range 8.5–9.0 (circles) only a lower limit, if any, for  $\Delta \log(\text{SFR})$  could be assumed from the present SDSS sample, leading to  $\log(\text{SFR}) < -1.5$ . In the case of the iso- $D_n(4000)$  line  $1.2 \leq D_n(4000) < 1.3$ , the value of the intersect position has been derived extrapolating slightly this iso- $D_n(4000)$ . The mean value of  $\Delta \log(\text{SFR})$  for each iso- $D_n(4000)$ , considering all the iso-masses, is shown in the coloured numbers (only lower limits of  $\Delta \log(\text{SFR})$  for the  $8.5 \leq \log(M_*/M_\odot) < 9.0$  mass range are not considered). The black dotted line indicates  $\Delta \log(\text{SFR}) = 0$ .

that the iso- $D_n(4000)$  line for  $1.1 \leq D_n(4000) < 1.2$  (green line in Fig. 2) represents the best approximation to the locus where the change of the relation between oxygen abundance and SFR is observed, for each stellar mass range and given SFR. Before this line, for  $D_n(4000)$  larger than 1.2, the slope of each O/H-SFR iso-mass line may be considered flat as its absolute value is smaller than 0.002.

This way, for all galaxies with stellar mass  $\log(M_*/M_\odot) \leq 10.5$ , the green iso- $D_n(4000)$  line defines, *de facto*, an effective *isochrone*, which marks the locus of the sudden change in the derivative of oxygen abundance against SFR in the sample galaxies. This plot may illustrate why the case for a universal negative relation between oxygen abundance and SFR is still controversial for some samples of galaxies. The exact region in which the negative slope of the metallicity – SFR relation may hold varies for each stellar mass range; a negative dependence of metallicity on SFR could be seen for a given galaxy mass range but only for those galaxies hosting the youngest stellar population (i.e.  $D_n(4000) \leq 1.1$ ). A similar behaviour can be observed in panel b) for  $\log(\text{N/O})$ . Again for galaxies with  $\log(M_*/M_\odot) \leq 11$  there is a mild, if any, dependence of  $\log(\text{N/O})$  on SFR, except when the green iso- $D_n(4000)$  line is reached. Beyond this point, moving towards larger SFR for a fixed stellar mass (i.e. along dash-dotted lines), a strong negative dependence of  $\Delta \log(\text{N/O})/\Delta \log(\text{SFR})$  is evident. The value of  $\log(\text{N/O})$  at which these changes in the slope can be seen from the typical values in dwarf galaxies up to the solar  $\log(\text{N/O})_\odot$ . The similar behaviour exhibited by the oxygen abundance and the nitrogen-to-oxygen abundance ratio against SFR, shown in both panels of Fig. 2, respectively, can give us some hints to understand the chemical evolution of our sample galaxies and the origin underlying of the MZRSFR relationship.

We have found respective loci in the planes  $12 + \log(\text{O/H}) - \text{SFR}$  and  $\log(\text{N/O}) - \text{SFR}$  delimiting two broad regions domains in these diagrams for the sample galaxies, in one of them the sample galaxies show a clear dependence of metallicity on the SFR, whereas in the corresponding complementary region no dependence is seen, along each galaxy stellar mass sequence. These loci appear well represented on each plot by the line corresponding to galaxies with  $D_n(4000) < 1.2$ , for which a mean stellar age younger than 150 Myr is expected (Mateus et al. 2006). Along these two loci lines, it seems that the precise oxygen abundance (N/O ratio) and SFR, for each galaxy stellar mass (i.e. specific SFR) appear to be tuned<sup>10</sup>, defining, *de facto*, the *effective isochrone* corresponding to the average stellar population for each galaxy. This applies only to galaxies with  $\log(M_*/M_\odot) \leq 10.5$ ; for more massive galaxies we do not observe this behaviour in our sample, since the lines of the  $D_n(4000)$  index converge at high metallicity (near solar to oversolar), and O/H and N/O do not show here observable decrease, suggesting an evolution without metallicity loss and mainly driven by galaxy mass.

In Fig. 5 we show the MZSFR relation for the star-forming galaxies with  $D_n(4000) < 1.2$  (panel a) and  $D_n(4000) \geq 1.2$  (panel b). From this figure, it can be seen that galaxies with young and old stellar populations are located in different domains in the MZSFR three dimensional diagram. As expected, galaxies with younger stellar populations ( $D_n(4000) < 1.2$ , represented as blue dots in the figure) are located in the zone where SFR is higher, at a fixed  $12 + \log(\text{O/H})$ . In contrast, galaxies with older stellar populations ( $D_n(4000) \geq 1.2$ , represented as red dots in the figure) fall in the area where SFR is lower, at fixed  $12 + \log(\text{O/H})$ . This plot has, however, a large dispersion, and therefore, we have analysed this possible dependence of the OH on SFR and on the stellar age from other point of view by using the classical method of representing residuals of a correlation as a function of other parameters. Thus, we plot three panels in Fig. 6. In the first one at the left, the MZR relation is drawn with a polynomial fit overplotted and, at the bottom, the residuals of this relation. In the middle panel, these same residuals are plotted as a function of the SFR, with a least-square straight line overplotted and the corresponding residuals at the bottom. These residuals, within  $\pm 0.2$  dex, are represented as a function of the  $D_n(4000)$  parameter in the right panel, where again a correlation appears. This way, a third parameter, the age, besides the stellar mass and the SFR, arises clearly as something to take into account in the analysis of the MZR-SFR. In fact, in this last panel, a fit with two straight lines may be also acceptable since, as we claim before, for  $D_n(4000) > 1.2$  the correlation is almost flat, while a strong slope would appear in the younger objects with  $D_n(4000) < 1.2$ .

Interestingly, a direct consequence of the above findings has been the selection of a sub-sample of galaxies which populate the youngest part of the two diagrams of Fig. 2. This group of (8598) galaxies are “outliers” of the sample, and cluster around the iso-line  $D_n(4000) < 1.1$ , on average in both panels of Fig. 2. It is for this group of very young galaxies for which the largest changes in the slopes of the O/H vs. SFR relation are observed (similar for N/O vs. SFR). The galaxies in this group are mainly but not only dwarf galaxies, they sample a range in galaxy stellar masses, as shown; but always showing the largest SFR measured for its stellar mass. This is easily appreciated in Fig. 7 where the relation between SFR and  $M_*$  for our sample of SDSS star-

<sup>10</sup> By tuned, we refer that the stellar age accompanies and it has to be taken into account in the mass-metallicity-SFR relation.



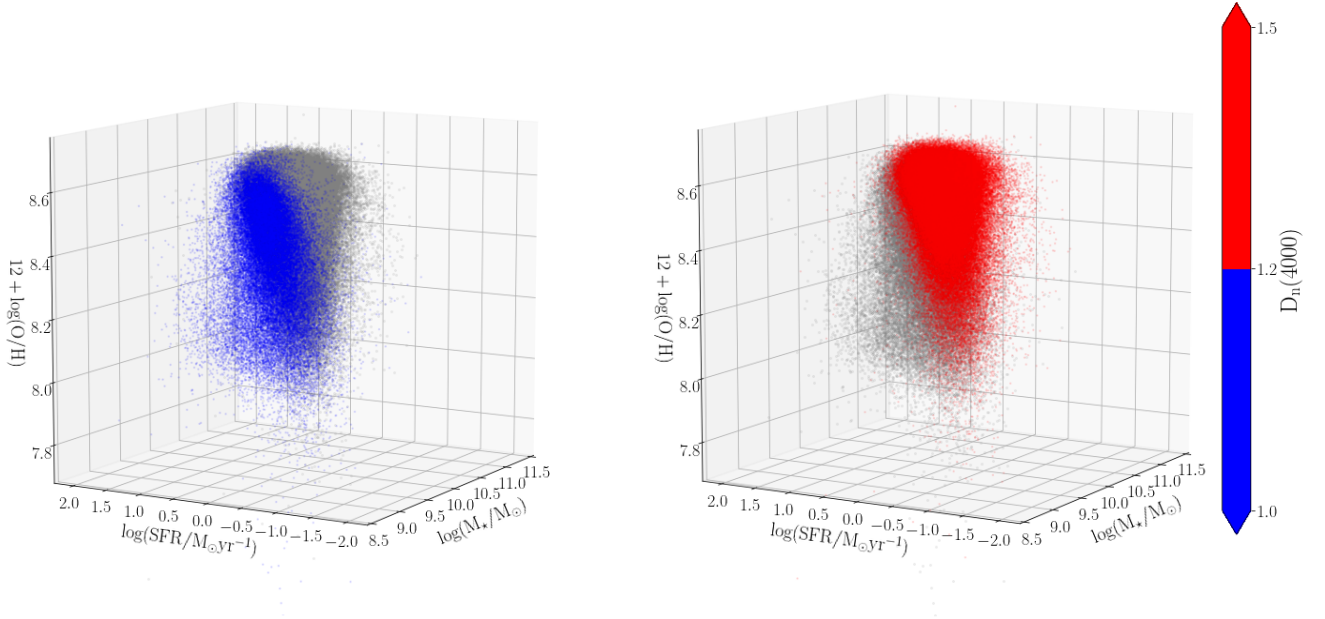


**Fig. 5.** MZSFR for star-forming galaxies corrected for aperture. Colour-coded star-forming galaxies with  $D_n(4000) < 1.2$  (blue in panel a, represented as grey in panel b) and  $D_n(4000) \geq 1.2$  (red in panel b, represented as grey in panel a). Note the scale of the SFR axis decreases towards the right in the figures.

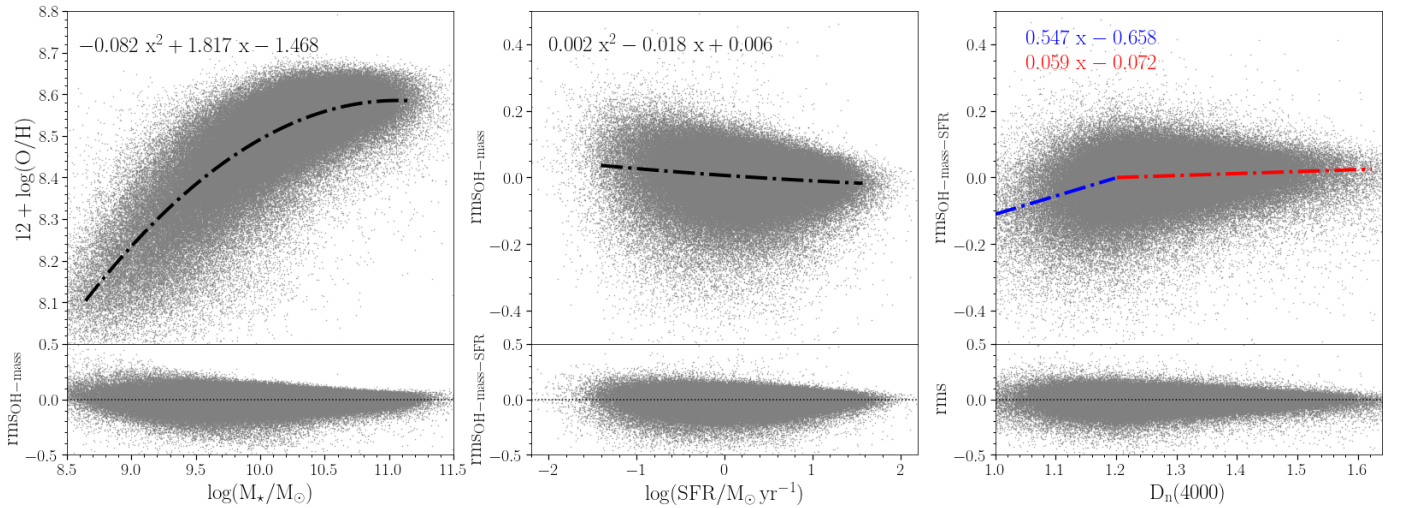


**Fig. 6.** a) MZSFR for our sample of galaxies, overplotted a line with a polynomial fit to these results. In the bottom the residuals data-fit,  $OH - OH_{fit,M}$  are represented as a function of the stellar mass; b) These residuals of  $OH - OH_{fit,M}$  as a function of the SFR with a minimum straight line fitting the points. The residual of this fit are represented at the bottom as a function of SFR; c) The residual of the later fit,  $OH - OH_{fit,M} - Res_{fit,SFR}$  as a function of the parameter  $D_n(4000)$ . In the upper panels, the correlation coefficients for each fit are shown in the top right.

forming galaxies is presented; galaxies are colour coded according to the  $D_n(4000)$  parameter. In this figure it can be seen that, for a fixed SFR nearly the entire range of  $D_n(4000)$  is covered, where the parameter  $D_n(4000)$  increases as the stellar mass increases, i.e. more massive galaxies have higher  $D_n(4000)$  values than less massive ones. Similarly, for each fixed stellar mass, a range in SFR is observed where the largest SFR corresponds to the youngest objects.

In order to explore the nature of these 8598 galaxies we have performed a sanity check in Appendix A to confirm their metallicity and SFR, (see Figures A.3, A.4, and A.5) and to gain more insight into the nature of this sub-sample of galaxies. We have checked that the abundances and SFR derived for these galaxies

were not affected by aperture corrections, performing a particular study of this subsample.

In Fig. 8 we summarise all the results concerning to O/H, SFR and age of the stellar populations, making use of the “population box”  $D_n(4000) - SFR - 12 + \log(O/H)$  three dimensional diagram, where values found for the star-forming galaxies are colour-coded according to the  $M_*$  of each galaxy as shown. A clear correlation between  $D_n(4000)$ , SFR and  $12 + \log(O/H)$  has been found. Galaxies with  $D_n(4000)$  values  $< 1.2$  span the range of stellar masses  $\log(M_*/M_\odot) = 8.5$  to  $11.5$ , where the majority of the sample galaxies have stellar masses less than  $\sim 10.5$ . The less massive galaxies ( $\log(M_*/M_\odot) \lesssim 9$ ) mostly have values of  $D_n(4000)$  less than  $1.2$ , and, as expected, have the low-

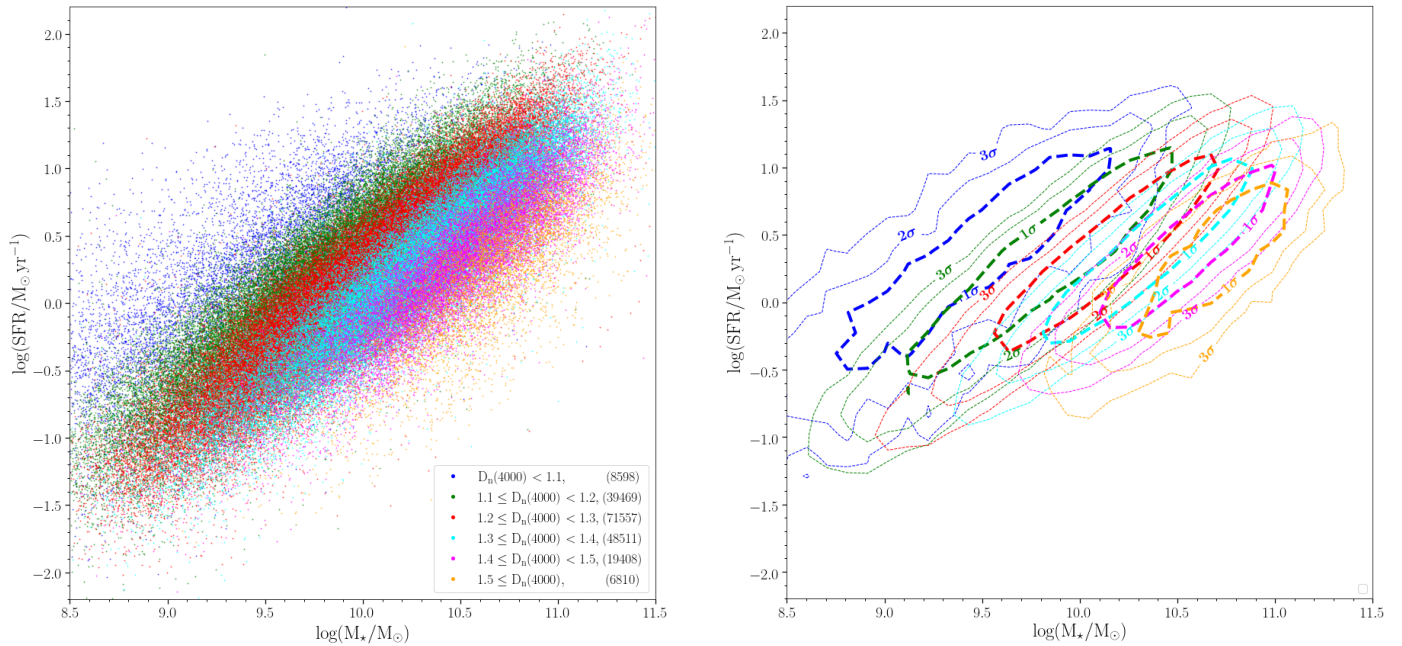


**Fig. 7.** Relation between SFR and  $M_*$  for star-forming galaxies colour coded according to the  $D_n(4000)$  parameter (left panel) and its corresponding confidence limits from  $1\sigma$  to  $3\sigma$  (right panel). All the points and contours of  $D_n(4000)$  parameter in the figures have the same colours as Fig. 2.

est  $12 + \log(\text{O}/\text{H})$ . On the other hand, the most massive galaxies ( $\log(M_*/M_\odot) \gtrsim 11$ ) are those with the highest  $12 + \log(\text{O}/\text{H})$  values (solar metallicity) and have  $D_n(4000)$  values higher than 1.1, although most galaxies have values above 1.2. According to the SFR– $M_*$  relation, the higher the stellar mass, the higher the SFR.

The apparent metallicity – SFR anticorrelation appears to be controversial in the literature; this relation has been interpreted as the consequence of a possible selection effect, and/or possibly resulting from the existence of massive infall of mainly metal poor gas on these galaxies, which would produce a strong enhancement of the SFR and, as a consequence, should dilute the metallicity of the interstellar medium (ISM) (Ellison et al. 2008; Mannucci et al. 2010; Yates et al. 2012) giving rise to an anticorrelation between  $12 + \log(\text{O}/\text{H})$  and SFR. This picture seems to be supported by some theoretical work (e.g. Sakstein et al. 2011; Dayal et al. 2013). Though recent observational work has questioned this scenario. We have shown in this work a deep and complex relation between the MZR and SFR which appears to be tuned to the mean age of the galaxy stellar population. The anticorrelation found between oxygen abundance and SFR appears to be significant only for those galaxies hosting the youngest stellar populations. The massive infall scenario, could be invoked to explain these high SFR objects; however for these galaxies we can see that  $\log(\text{N}/\text{O})$  – SFR also anticorrelate, suggesting a framework more complex than the standard infall scenario where N/O should not be much affected. Further deep spectroscopic observations of the extreme SFR sub-sample could provide valuable information to in order to understand the evolution of this very active star-forming galaxies.

#### 4. Summary and conclusions

In this work we have derived O/H and N/O corrected for aperture effects. These empirical aperture corrections are based on the sample of 165 spiral galaxies from the CALIFA project Iglesias-Páramo et al. (2016). We studied the O/H – SFR and N/O – SFR

relations, as well as their relation with the parameter  $D_n(4000)$ , a proxy of the age of the stellar populations of the galaxies. We compared the location in the SFR –  $M_*$  and MZSFR diagrams of the star-forming galaxies according to its value of the  $D_n(4000)$  for each galaxy.

Our main conclusions are the following:

- i) A robust stellar mass – metallicity relation (MZR) locus has been derived consistent with the “anchoring” points of a selected set of well studied nearby galaxies with a direct derivation of abundance. A complex relation between MZR and SFR across the whole range of galaxy mass and metallicity has been observed, showing a pattern of slope changes of the MZR – SFR relation in the O/H versus SFR plane, which appears tuned to the age of the stellar population of the galaxies.
- ii) From the study of the relation between the MZR and SFR, a new dependence between O/H – SFR has been found with the age of the galaxies’ stellar populations. The dependence between the MZR and SFR is strong mainly for star-forming galaxies with high SFR and low  $D_n(4000)$ . Galaxies with older stellar populations ( $D_n(4000) \geq 1.2$ ) and massive ( $\log(M_*/M_\odot) \gtrsim 10.5$ ) tend to saturate, and seem to flatten in the O/H – SFR relation when  $12 + \log(\text{O}/\text{H}) \geq 8.55$ , irrespective of their SFR; which indicates that the metallicity remains constant only depending on the stellar mass of these massive galaxies. We also observe a dependence between N/O – SFR with the age of the galaxies’ stellar populations, where those galaxies with oldest stellar populations and massive seem to flatten when  $\log(\text{N}/\text{O}) \geq -0.9$ .
- iii) On the contrary, for galaxies with younger stellar populations ( $D_n(4000) < 1.2$ ), a negative dependence has been found between O/H and SFR (also for N/O and SFR) for less massive galaxies ( $\log(M_*/M_\odot) \lesssim 10.5$ ). This anticorrelation has been interpreted as the existence of massive infall of mainly metal poor gas on the galaxies, which would produce a strong enhancement of the SFR and, as a con-

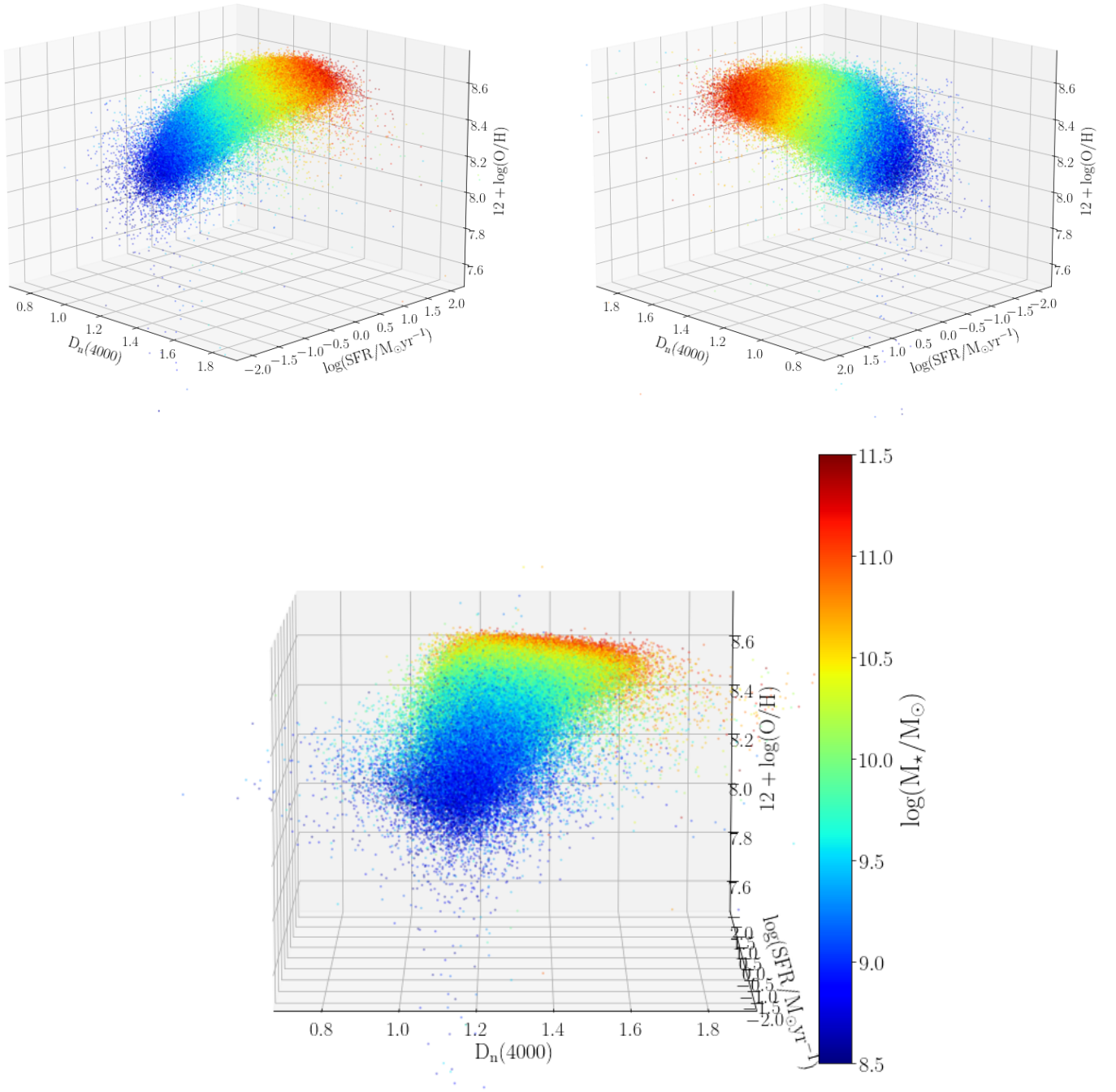


**Fig. 8.** Population box ( $D_n(4000)$  – SFR –  $12+\log(\text{O}/\text{H})$  diagram) for our sample of star-forming galaxies colour coded by  $M_*$ .

sequence, should dilute the metallicity of the interstellar medium (ISM).

- iv) This negative dependence found between O/H and SFR for galaxies with younger stellar populations holds in a metallicity range from typical dwarf values to solar values, covering a wide range of stellar masses, suggesting that galaxies with young stellar populations are not only composed of dwarf galaxies. These young galaxies of our SDSS sam-

ple always show the highest SFR measured for their stellar mass.

- v) Galaxies with young and old stellar populations are located in different domains in the three dimensional MZSFR diagram: i) galaxies with younger stellar populations ( $D_n(4000) < 1.2$ ) are located in the zone where SFR is higher, at fixed  $12+\log(\text{O}/\text{H})$ ; and ii) galaxies with older



stellar populations ( $D_n(4000) \geq 1.2$ ) fall in the area where SFR is lower, at fixed  $12+\log(\text{O}/\text{H})$ .

We have found a population of outliers galaxies in the O/H – SFR relation (and also in the N/O – SFR relation), with young stellar population ages. Further characterisation of the physical and chemical properties of these galaxies is necessary to understand how they evolve chemically and to unravel the O/H and N/O relation for these galaxies.

**Acknowledgements.** We thank the anonymous referee for very constructive suggestions that have helped us to improve this manuscript. SDP is grateful to the Fonds de Recherche du Québec - Nature et Technologies. SDP, JVM, JIP, CK, and EPM acknowledge financial support from the Spanish Ministerio de Economía y Competitividad under grants AYA2016-79724-C4-4-P and PID2019-107408GB-C44, from Junta de Andalucía Excellence Project P18-FR-2664, and also acknowledge support from the State Agency for Research of the Spanish MCIU through the ‘Center of Excellence Severo Ochoa’ award for the Instituto de Astrofísica de Andalucía (SEV-2017-0709). L.S.P acknowledges support within the framework of the program of the NAS of Ukraine Support for the development of priority fields of scientific research (CPCEL 6541230). I.A.Z acknowledges support by the National Academy of Sciences of Ukraine under the Research Laboratory Grant for young scientists No. 0120U100148. Funding for SDSS-III has been provided by the Alfred P. Sloan Foundation, the Participating Institutions, the National Science Foundation, and the U.S. Department of Energy Office of Science. The SDSS-III web site is <http://www.sdss3.org>. This study makes use of the results based on the Calar Alto Legacy Integral Field Area (CALIFA) survey (<http://califa.caha.es/>). This research made use of Python (<http://www.python.org>) and IPython (Pérez & Granger 2007); APLpy (Robitaille & Bressert 2012); Numpy (Van Der Walt et al. 2011); Pandas (McKinney 2010); of Matplotlib (Hunter 2007), a suite of open-source Python modules that provides a framework for creating scientific plots. This research made use of Astropy, a community-developed core Python package for Astronomy (Astropy Collaboration et al. 2013). The Astropy web site is <http://www.astropy.org>.

## References

- Alam, S., Albareti, F. D., Allende Prieto, C., et al. 2015, *ApJS*, 219, 12
- Andrews, B. H. & Martini, P. 2013, *ApJ*, 765, 140
- Arellano-Córdova, K. Z., Esteban, C., García-Rojas, J., & Méndez-Delgado, J. E. 2021, *MNRAS*, 502, 225
- Asplund, M., Grevesse, N., Sauval, A. J., & Scott, P. 2009, *ARA&A*, 47, 481
- Astropy Collaboration, Robitaille, T. P., Tollerud, E. J., et al. 2013, *A&A*, 558, A33
- Balogh, M. L., Morris, S. L., Yee, H. K. C., Carlberg, R. G., & Ellingson, E. 1999, *ApJ*, 527, 54
- Barrera-Ballesteros, J. K., Heckman, T., Sánchez, S. F., et al. 2018, *ApJ*, 852, 74
- Barrera-Ballesteros, J. K., Sánchez, S. F., Heckman, T., Blanc, G. A., & The MaNGA Team. 2017, *ApJ*, 844, 80
- Barrera-Ballesteros, J. K., Utomo, D., Bolatto, A. D., et al. 2020, *MNRAS*, 492, 2651
- Belfiore, F., Maiolino, R., Maraston, C., et al. 2016, *MNRAS*, 461, 3111
- Berg, D. A., Skillman, E. D., Croxall, K. V., et al. 2015, *ApJ*, 806, 16
- Bresolin, F., Kudritzki, R.-P., Urbaneja, M. A., et al. 2016, *ApJ*, 830, 64
- Brinchmann, J., Charlot, S., White, S. D. M., et al. 2004, *MNRAS*, 351, 1151
- Brown, J. S., Martini, P., & Andrews, B. H. 2016, *MNRAS*, 458, 1529
- Bundy, K., Bershady, M. A., Law, D. R., et al. 2015, *ApJ*, 798, 7
- Chabrier, G. 2003, *ApJ*, 586, L133
- Cook, D. O., Dale, D. A., Johnson, B. D., et al. 2014, *MNRAS*, 445, 899
- Cresci, G., Mannucci, F., & Curti, M. 2019, *A&A*, 627, A42
- Cresci, G., Mannucci, F., Sommariva, V., et al. 2012, *MNRAS*, 421, 262
- Croxall, K. V., Pogge, R. W., Berg, D. A., Skillman, E. D., & Moustakas, J. 2016, *ApJ*, 830, 4
- Curti, M., Cresci, G., Mannucci, F., et al. 2017, *MNRAS*, 465, 1384
- Curti, M., Mannucci, F., Cresci, G., & Maiolino, R. 2020, *MNRAS*, 491, 944
- Davé, R., Finlator, K., & Oppenheimer, B. D. 2011, *MNRAS*, 416, 1354
- Dayal, P., Ferrara, A., & Dunlop, J. S. 2013, *MNRAS*, 430, 2891
- De Rossi, M. E., Bower, R. G., Font, A. S., Schaye, J., & Theuns, T. 2017, *MNRAS*, 472, 3354
- Duarte Puertas, S., Vilchez, J. M., Iglesias-Páramo, J., et al. 2017, *A&A*, 599, A71
- Edmunds, M. G. & Pagel, B. E. J. 1978, *MNRAS*, 185, 77P
- Ellison, S. L., Patton, D. R., Simard, L., & McConnachie, A. W. 2008, *ApJ*, 672, L107
- Ellison, S. L., Simard, L., Cowan, N. B., et al. 2009, *MNRAS*, 396, 1257
- Fernández-Martín, A., Pérez-Montero, E., Vilchez, J. M., & Mampaso, A. 2017, *A&A*, 597, A84
- Finlator, K. & Davé, R. 2008, *MNRAS*, 385, 2181
- Fisher, D. B. & Drory, N. 2011, *ApJ*, 733, L47
- Gallazzi, A., Charlot, S., Brinchmann, J., White, S. D. M., & Tremonti, C. A. 2005, *MNRAS*, 362, 41
- García-Benito, R., Zibetti, S., Sánchez, S. F., et al. 2015, *A&A*, 576, A135
- Garnett, D. R. 2002, *ApJ*, 581, 1019
- Gomes, J. M., Papaderos, P., Vilchez, J. M., et al. 2016, *A&A*, 586, A22
- Hernandez, S., Larsen, S., Aloisi, A., et al. 2019, *ApJ*, 872, 116
- Hughes, T. M., Cortese, L., Boselli, A., Gavazzi, G., & Davies, J. I. 2013, *A&A*, 550, A115
- Hunt, L., Dayal, P., Magrini, L., & Ferrara, A. 2016, *MNRAS*, 463, 2002
- Hunter, J. D. 2007, *Computing In Science & Engineering*, 9, 90
- Iglesias-Páramo, J., Vilchez, J. M., Galbany, L., et al. 2013, *A&A*, 553, L7
- Iglesias-Páramo, J., Vilchez, J. M., Rosales-Ortega, F. F., et al. 2016, *ApJ*, 826, 71
- Kang, X., Zhang, F., Chang, R., Wang, L., & Cheng, L. 2016, *A&A*, 585, A20
- Kashino, D., Renzini, A., Silverman, J. D., & Daddi, E. 2016, *ApJ*, 823, L24
- Kauffmann, G., Heckman, T. M., White, S. D. M., et al. 2003, *MNRAS*, 341, 33
- Kojima, T., Ouchi, M., Nakajima, K., et al. 2017, *PASJ*, 69, 44
- Kroupa, P. 2001, *MNRAS*, 322, 231
- Kudritzki, R.-P., Urbaneja, M. A., Gazak, Z., et al. 2012, *ApJ*, 747, 15
- Lara-López, M. A., Bongiovanni, A., Cepa, J., et al. 2010a, *A&A*, 519, A31
- Lara-López, M. A., Cepa, J., Bongiovanni, A., et al. 2010b, *A&A*, 521, L53
- Lee, H., Skillman, E. D., Cannon, J. M., et al. 2006, *ApJ*, 647, 970
- Lequeux, J., Peimbert, M., Rayo, J. F., Serrano, A., & Torres-Peimbert, S. 1979, *A&A*, 80, 155
- Licquia, T. C. & Newman, J. A. 2015, *ApJ*, 806, 96
- Magrini, L., Gonçalves, D. R., & Vajgel, B. 2017, *MNRAS*, 464, 739
- Maiolino, R. & Mannucci, F. 2019, *A&A Rev.*, 27, 3
- Mannucci, F., Cresci, G., Maiolino, R., Marconi, A., & Gnerucci, A. 2010, *MNRAS*, 408, 2115
- Mast, D., Rosales-Ortega, F. F., Sánchez, S. F., et al. 2014, *A&A*, 561, A129
- Mateus, A., Sodré, L., Cid Fernandes, R., et al. 2006, *MNRAS*, 370, 721
- McKinney, W. 2010, in *Proceedings of the 9th Python in Science Conference*, ed. S. van der Walt & J. Millman, 51 – 56
- Mollá, M., Vilchez, J. M., Gavilán, M., & Díaz, A. I. 2006, *MNRAS*, 372, 1069
- Møller, P., Fynbo, J. P. U., Ledoux, C., & Nilsson, K. K. 2013, *MNRAS*, 430, 2680
- Mouchine, M., Gibson, B. K., Renda, A., & Kawata, D. 2008, *A&A*, 486, 711
- Okamoto, T., Nagashima, M., Lacey, C. G., & Frenk, C. S. 2017, *MNRAS*, 464, 4866
- Peng, Y.-j. & Maiolino, R. 2014, *MNRAS*, 438, 262
- Pérez, F. & Granger, B. E. 2007, *Computing in Science and Engineering*, 9, 21
- Pérez-Montero, E. 2014, *MNRAS*, 441, 2663
- Pérez-Montero, E. & Contini, T. 2009, *MNRAS*, 398, 949
- Pérez-Montero, E., Contini, T., Lamareille, F., et al. 2013, *A&A*, 549, A25
- Petropoulou, V., Vilchez, J., & Iglesias-Páramo, J. 2012, *ApJ*, 749, 133
- Petropoulou, V., Vilchez, J., Iglesias-Páramo, J., et al. 2011, *ApJ*, 734, 32
- Pilyugin, L. S. & Grebel, E. K. 2016, *MNRAS*, 457, 3678
- Pilyugin, L. S., Grebel, E. K., Zinchenko, I. A., Nefedyev, Y. A., & Mattsson, L. 2017, *MNRAS*, 465, 1358
- Pilyugin, L. S., Lara-López, M. A., Grebel, E. K., et al. 2013, *MNRAS*, 432, 1217
- Pilyugin, L. S., Thuan, T. X., & Vilchez, J. M. 2003, *A&A*, 397, 487
- Pilyugin, L. S., Thuan, T. X., & Vilchez, J. M. 2007, *MNRAS*, 376, 353
- Pilyugin, L. S., Vilchez, J. M., & Contini, T. 2004, *A&A*, 425, 849
- Pilyugin, L. S., Vilchez, J. M., Mattsson, L., & Thuan, T. X. 2012, *MNRAS*, 421, 1624
- Robitaille, T. & Bressert, E. 2012, *APLpy: Astronomical Plotting Library in Python*, Astrophysics Source Code Library
- Romeo Velonà, A. D., Sommer-Larsen, J., Napolitano, N. R., et al. 2013, *ApJ*, 770, 155
- Sackett, P. D. 1997, *ApJ*, 483, 103
- Sakstein, J., Pipino, A., Devriendt, J. E. G., & Maiolino, R. 2011, *MNRAS*, 410, 2203
- Salim, S., Lee, J. C., Ly, C., et al. 2014, *ApJ*, 797, 126
- Salim, S., Rich, R. M., Charlot, S., et al. 2007, *ApJS*, 173, 267
- Sánchez, S. F. 2020, *ARA&A*, 58, annurev
- Sánchez, S. F., Barrera-Ballesteros, J. K., López-Cobá, C., et al. 2019, *MNRAS*, 484, 3042
- Sánchez, S. F., Barrera-Ballesteros, J. K., Sánchez-Menguiano, L., et al. 2017, *MNRAS*, 469, 2121
- Sánchez, S. F., Kennicutt, R. C., Gil de Paz, A., et al. 2012, *A&A*, 538, A8
- Sánchez, S. F., Rosales-Ortega, F. F., Jungwiert, B., et al. 2013, *A&A*, 554, A58
- Sánchez-Menguiano, L., Sánchez Almeida, J., Muñoz-Tuñón, C., & Sánchez, S. F. 2020, *arXiv e-prints*, arXiv:2009.14211
- Skibba, R. A., Engelbracht, C. W., Dale, D., et al. 2011, *ApJ*, 738, 89
- Telford, O. G., Dalcanton, J. J., Skillman, E. D., & Conroy, C. 2016, *ApJ*, 827, 35
- Torrey, P., Vogelsberger, M., Hernquist, L., et al. 2018, *MNRAS*, 477, L16
- Tremonti, C. A., Heckman, T. M., Kauffmann, G., et al. 2004, *ApJ*, 613, 898
- Tsamis, Y. G., Walsh, J. R., Vilchez, J. M., & Péquignot, D. 2011, *MNRAS*, 412, 1367
- Van Der Walt, S., Colbert, S. C., & Varoquaux, G. 2011, *ArXiv e-prints*
- Vila-Costas, M. B. & Edmunds, M. G. 1992, *MNRAS*, 259, 121
- Vilchez, J. M., Relaño, M., Kennicutt, R., et al. 2019, *MNRAS*, 483, 4968
- Yates, R. M., Kauffmann, G., & Guo, Q. 2012, *MNRAS*, 422, 215
- Yin, J., Hou, J. L., Prantzos, N., et al. 2009, *A&A*, 505, 497
- Zahid, H. J., Dima, G. I., Kudritzki, R.-P., et al. 2014, *ApJ*, 791, 130
- Zurita, A. & Bresolin, F. 2012, *MNRAS*, 427, 1463

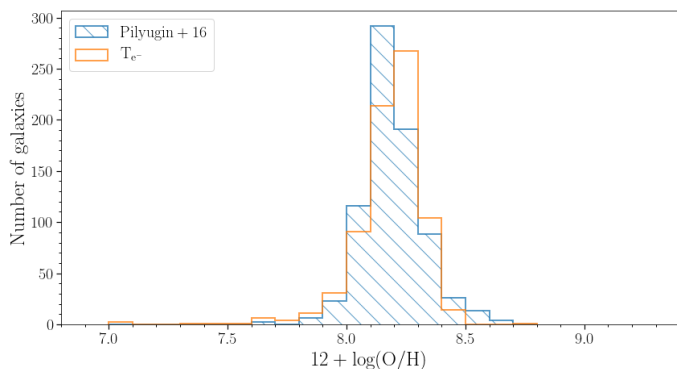


**Fig. A.1.** Distribution of oxygen abundance for SDSS star-forming galaxies with  $S/N([OIII]\lambda 4363) > 5$  using Pi16 methodology (blue dashed histogram) and using direct (electron temperature based) methodology (orange open histogram).

ures A.3, A.4, and A.5, to gain more insight into the nature of this sub-sample of galaxies. In Figs. A.4 and A.5 the spectra and SDSS three-colour images of 21 selected galaxies are shown. By focusing on the spectra of the galaxies found in the iso-mass [9, 9.5] (galaxies 6, 11, and 13) it can be observed how excitation decreases as the age of the galaxy’s stellar populations, and  $12+\log(O/H)$  increases. In the *isochrone*  $D_n(4000) < 1.1$  the spectra of these three galaxies (galaxies 4, 11, and 15) look similar, while their morphologies are different.

## Appendix A: Supplementary material

In this appendix the  $O/H - SFR$  relation as a function of the  $M_\star$  and the parameter  $D_n(4000)$  for the galaxies in Fig. 2 is shown in detail. From the  $O/H - SFR$  relation, a subsample of 21 galaxies is randomly defined in selected zones below the *isochrone*  $D_n(4000) \leq 1.2$ . Its location on the  $SFR - M_\star$  diagram and its spectra and SDSS three-colour images are shown. An upcoming more detailed study on the characterisation of this subsample of galaxies will be presented in a forthcoming work (Duarte Puertas et al. in prep.).

We have checked the SFR derived for these galaxies, confirming that these values were not produced by aperture corrections since the correction applied to these outliers was in fact smaller than average. We have searched and extracted the fluxes of the measured SDSS spectra and have verified for all these galaxies with electron temperature (i.e. with  $S/N([OIII]\lambda 4363) > 5$ ) that their direct (electron temperature based) abundances agree with our oxygen abundance values to within  $\sim 0.025$  dex on average (see Fig. A.1), as expected.

Fig. A.2 shows a density plot of our aperture corrected  $O/H$  versus SFR in six ranges of  $D_n(4000)$ . In each range of  $D_n(4000)$ , the density plot of the  $O/H - SFR$  relation of the galaxies in that interval is shown and the contours  $1\sigma$ ,  $2\sigma$  and  $3\sigma$  in each bin are represented, highlighting the fit to the running median.

Fig. A.3 shows again the aperture corrected  $O/H - SFR$  relation (left panel) and the aperture corrected  $SFR - M_\star$  relation (right panel). Since a population of galaxies has been found in the zone where  $O/H$  dilution occurs, we have defined there a subsample of 21 galaxies randomly selected, distributed below the *isochrone*  $1.1 < D_n(4000) \leq 1.2$  in the  $O/H - SFR$  diagram. We have done the selection in that way that some of them must be found in the *isochrones* of  $D_n(4000) < 1.1$  and others in  $1.1 < D_n(4000) \leq 1.2$ , as well as in the iso-mass [9, 9.5]. The positions of the 21 galaxies, as well as the position of the subsample of galaxies that have values of  $D_n(4000) < 1.2$  (blue color) and that of  $D_n(4000) \geq 1.2$  (red color), are also shown in the  $SFR - M_\star$  relation. Galaxies with values of  $D_n(4000) < 1.2$  (found in the lower right of the  $O/H - SFR$  diagram) are located in the upper left of the  $SFR - M_\star$  diagram. As expected from Fig. 2, galaxies with younger stellar populations have higher SFR values than older ones at a given stellar mass.

As said in the main text, in order to explore the nature of this subsample of 8598 galaxies, we have performed a sanity check to confirm their metallicity and SFR, such as we show in Fig-

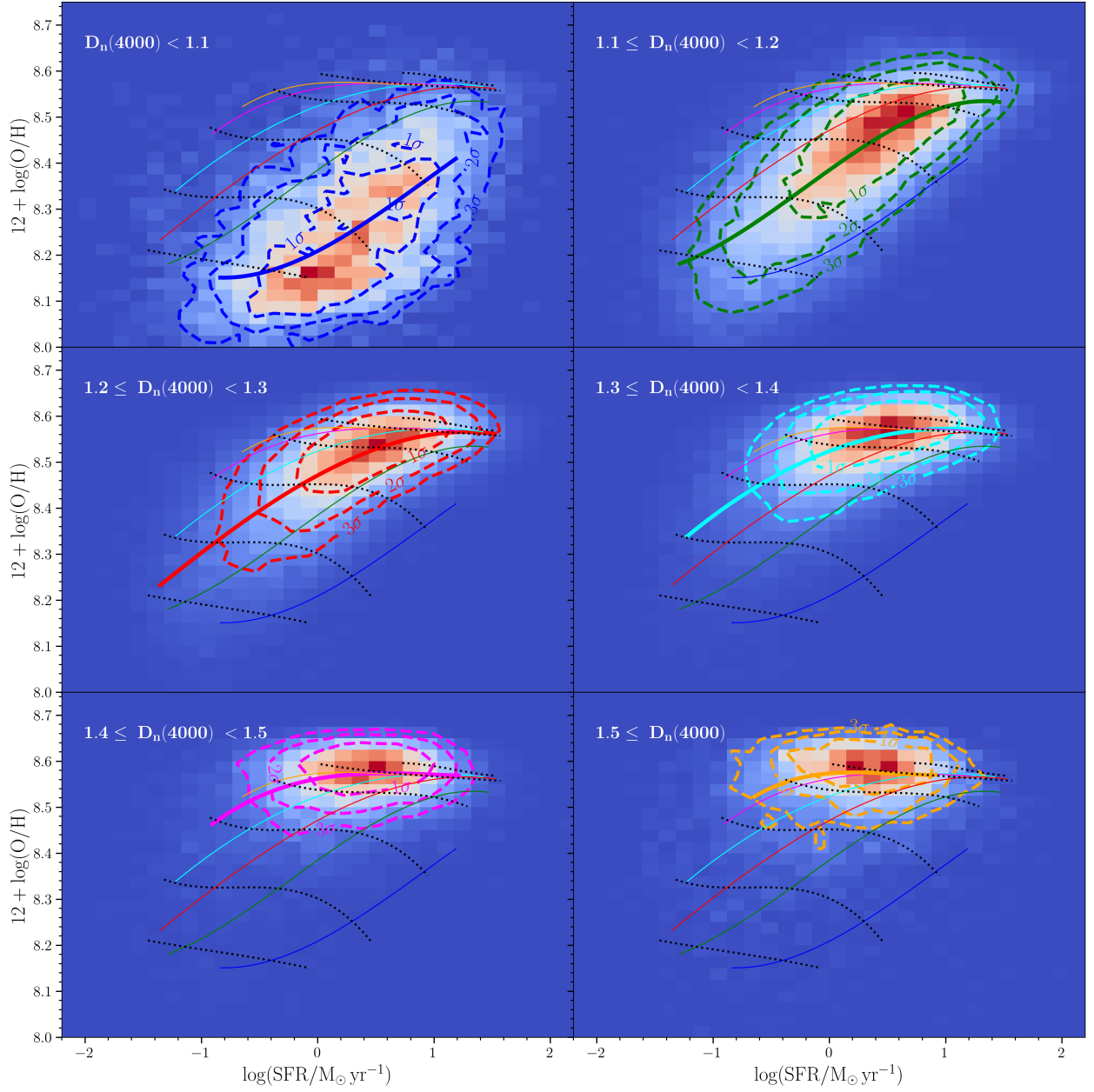


**Fig. A.2.** Detailed analysis of the  $12 + \log(\text{O}/\text{H})$  – SFR density plot presenting confidence limits for each  $D_n(4000)$  bin. Density plots for the relation between the  $12 + \log(\text{O}/\text{H})$  and SFR for star-forming galaxies for six  $D_n(4000)$  ranges. All the lines have the same colours as in Fig. 2. The dashed lines represent the  $1\sigma$ ,  $2\sigma$ , and  $3\sigma$  contours in each  $D_n(4000)$  bin.



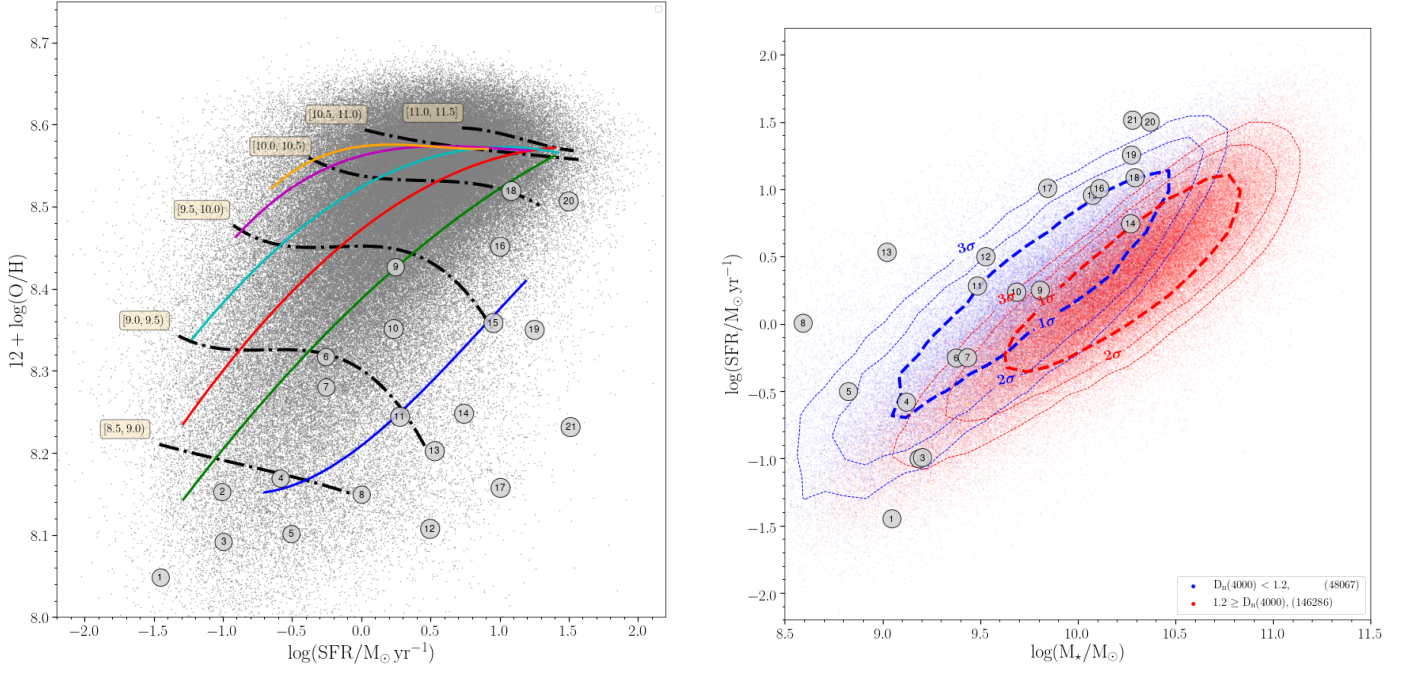


**Fig. A.3.** Selection of 21 galaxies from the  $12+\log(\text{O}/\text{H})$  vs. SFR diagram. Left panel) Relation between  $12+\log(\text{O}/\text{H})$  and SFR for star-forming galaxies. All the lines have the same colours as Fig. 2. A sample of 21 galaxies has been selected (as an example) in this diagram, the positions are represented with grey circles and have been labelled from 1 to 21 according to their SFR. Right panel) Relation between SFR and  $M_{\star}$  for star-forming galaxies. The points have been colour coded according to their  $D_n(4000)$ , blue if  $D_n(4000) < 1.2$  and red if  $D_n(4000) \geq 1.2$ . The dashed lines represent the  $1\sigma$ ,  $2\sigma$ , and  $3\sigma$  contours in each  $D_n(4000)$  sub-sample. Grey circles show the position in the SFR- $M_{\star}$  diagram of the 21 galaxies.

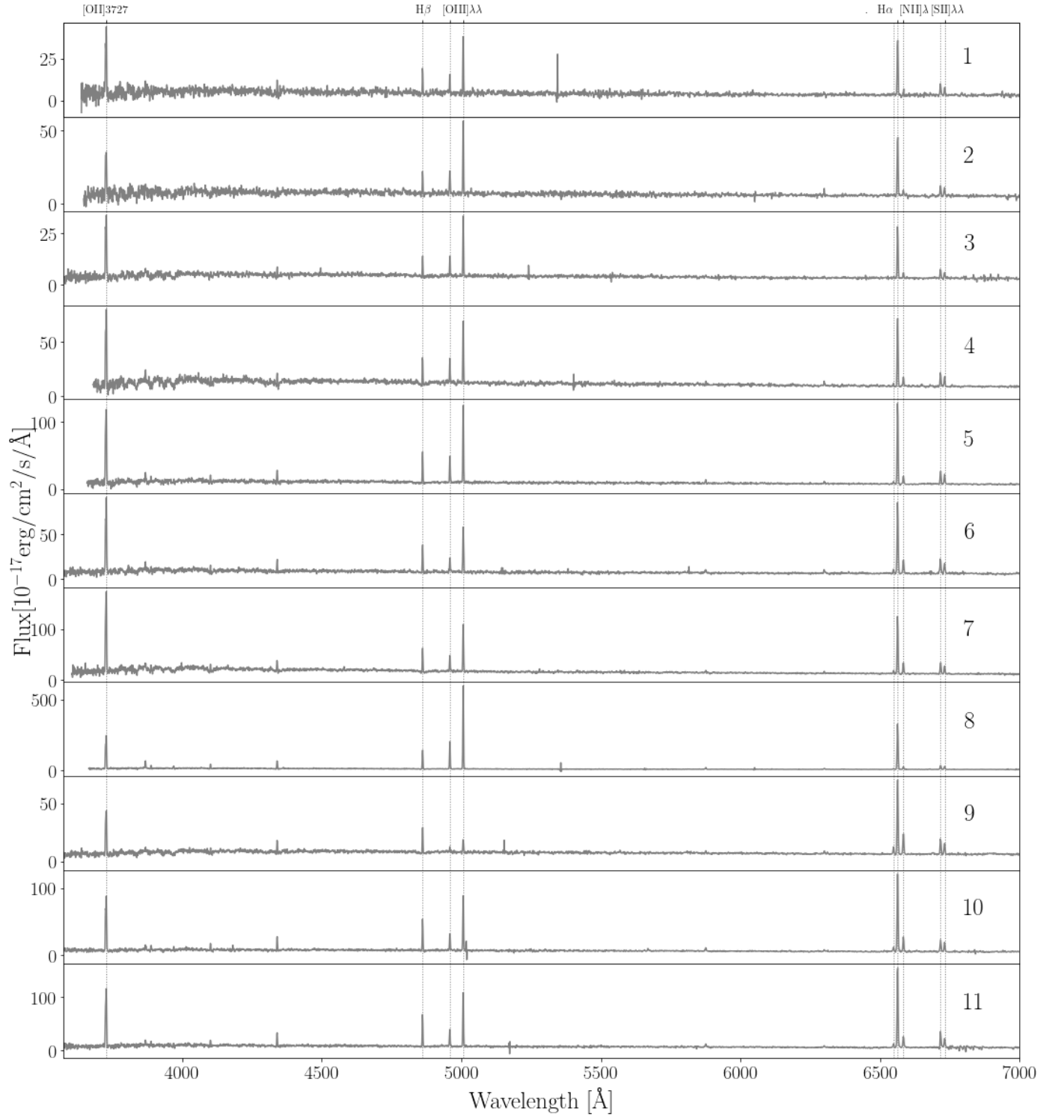


**Fig. A.4.** Spectra of the 21 galaxies defined in Fig. A.3. Grey dotted lines show the location of the emission lines studied in this paper. The galaxy label is indicated in each panel (right part).

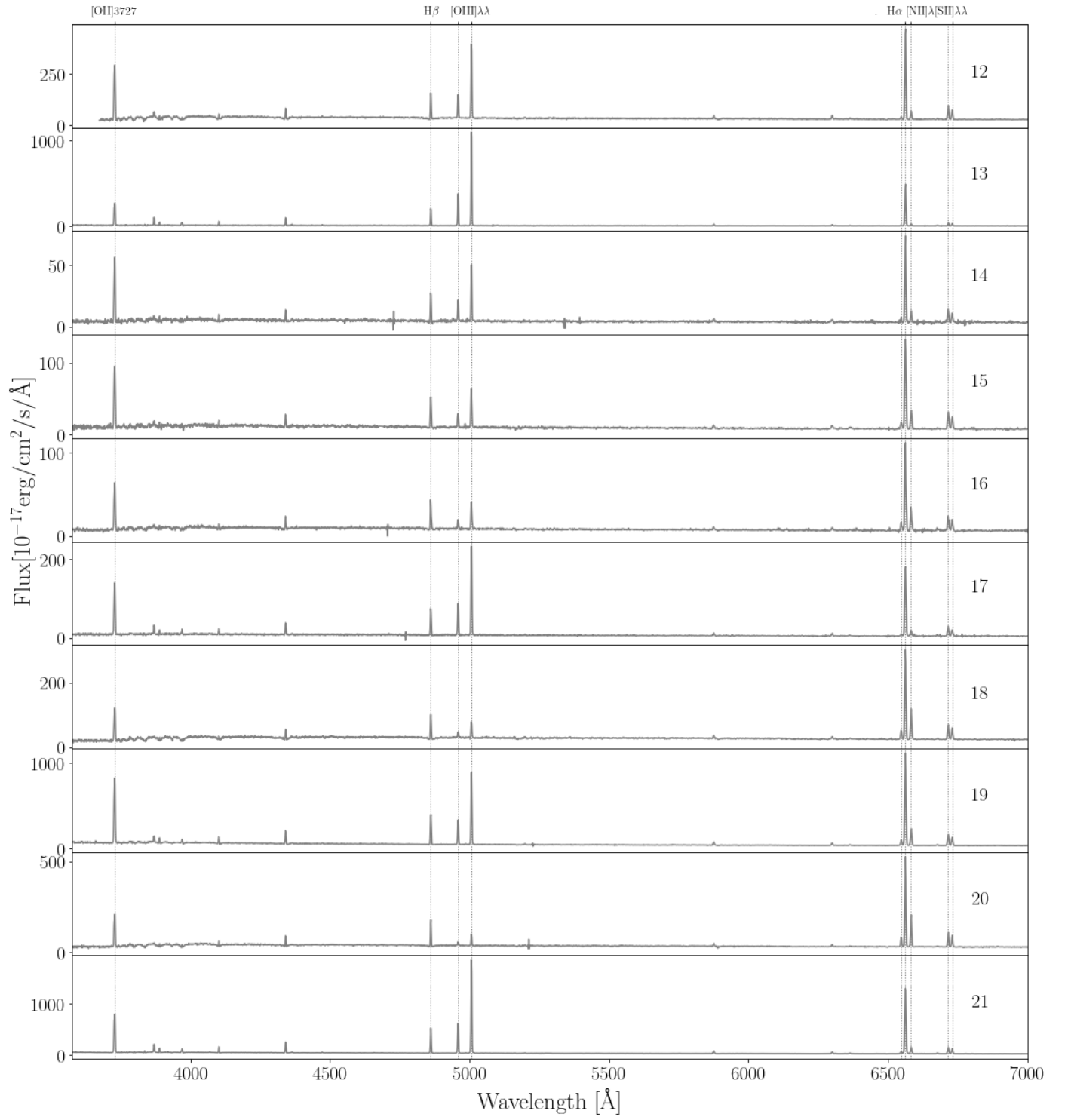
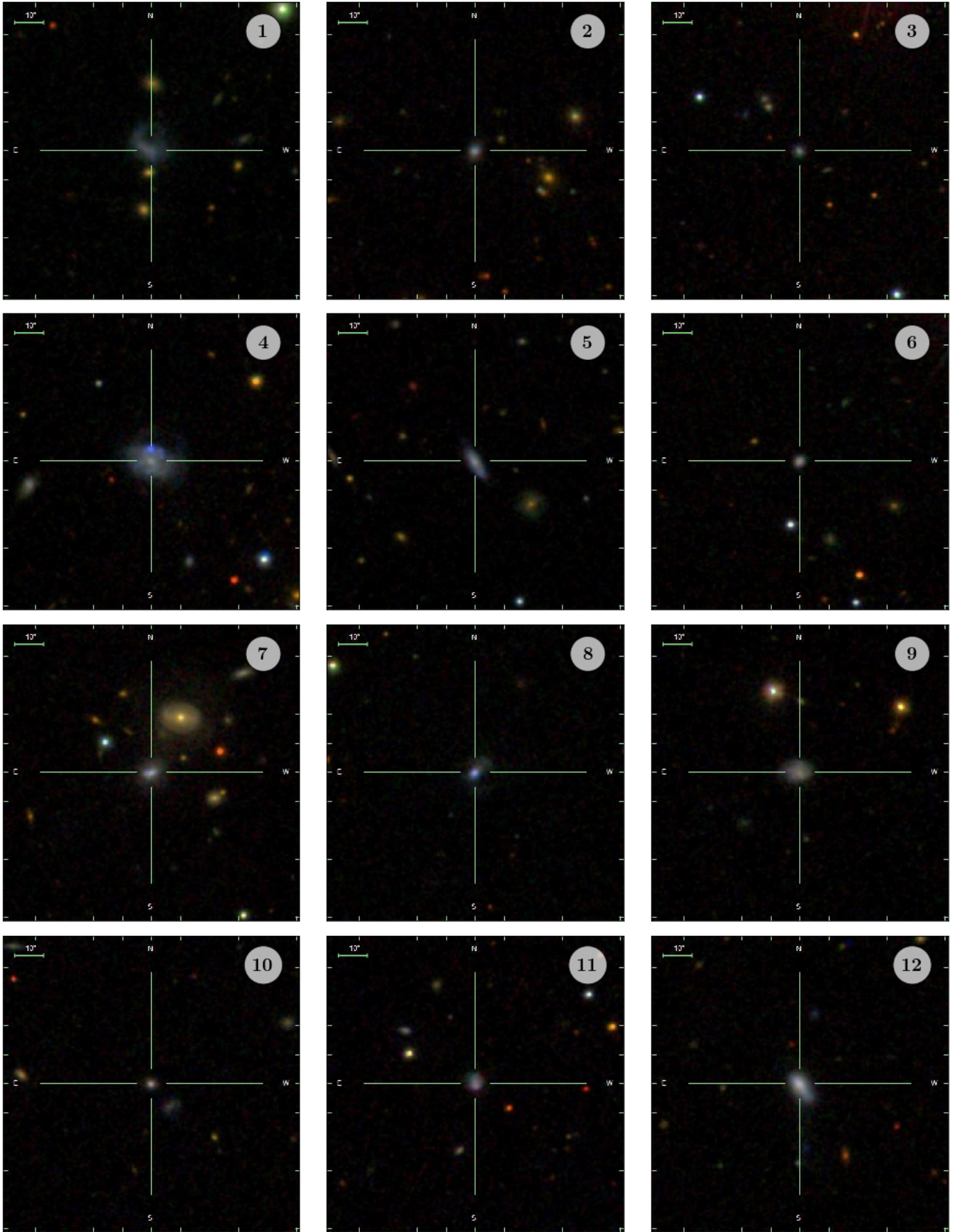
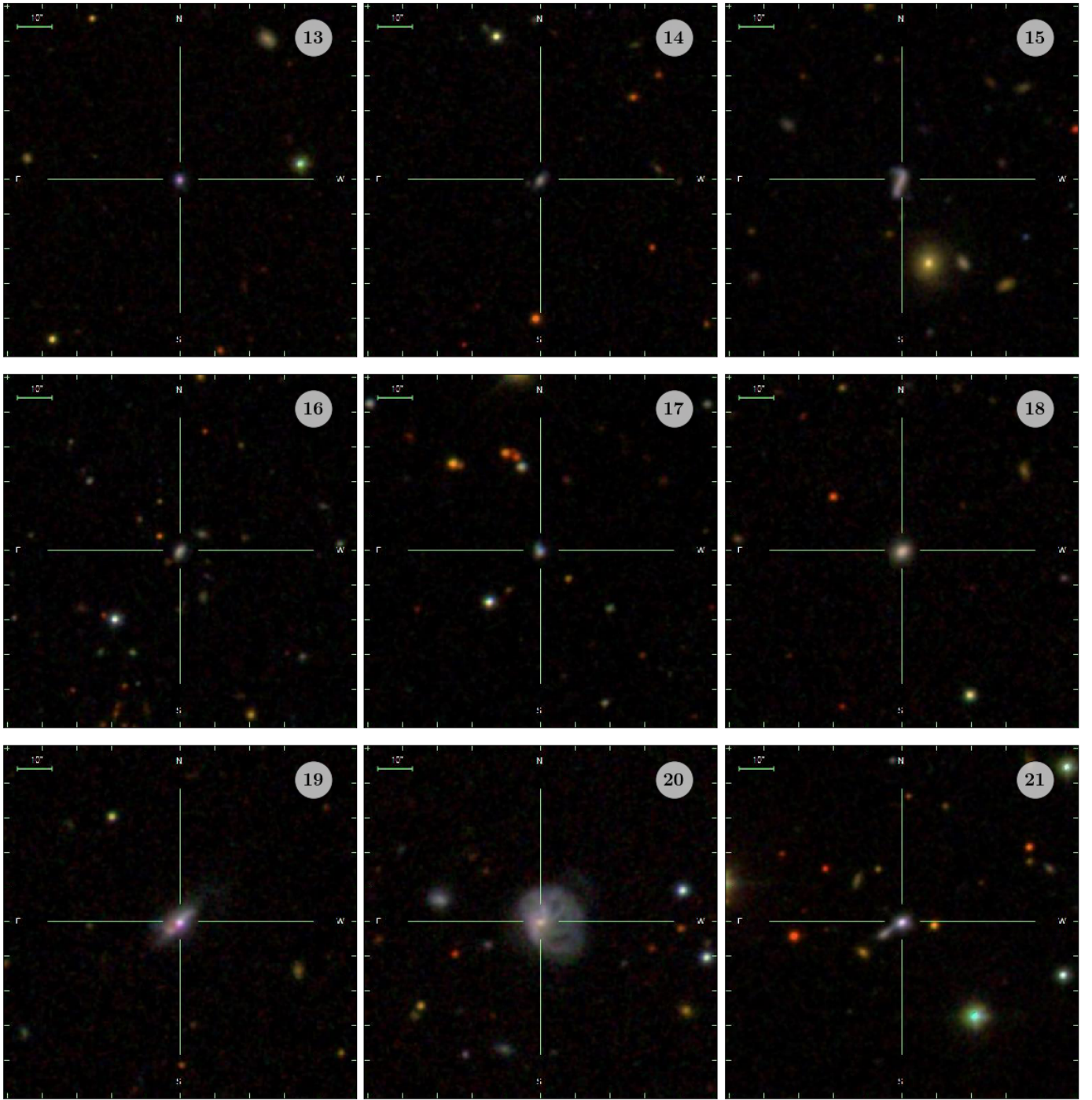


Fig. A.4. continued.





**Fig. A.5.** SDSS three-colour images of 21 galaxies defined in Fig. A.3 in the SDSS-DR12 footprint. North is up and East is left. The galaxy label is indicated in each panel (upper right).



**Fig. A.5.** continued.